

Three-Nucleon Dynamics in the dp breakup collisions at 190 MeV/nucleon using the WASA detector at COSY-Jülich

P. Adlarson,¹ W. Augustyniak,² W. Bardan,³ M. Bashkanov,⁴ F.S. Bergmann,⁵ M. Berłowski,⁶ A. Bondar,⁷ M. Büscher,^{8,9} H. Calén,¹ I. Ciepał,¹⁰ H. Clement,^{11,12} E. Czerwiński,³ K. Demmich,⁵ R. Engels,¹³ A. Erven,¹⁴ W. Eyrich,¹⁵ P. Fedorets,¹⁶ K. Föhl,¹⁷ K. Fransson,¹ F. Goldenbaum,^{13,*} A. Goswami,^{13,18} K. Grigoryev,^{13,*} L. Heijkenskjöld,^{1,†} V. Hejny,¹³ L. Jarczyk,^{3,‡} T. Johansson,¹ B. Kamys,³ G. Kemmerling,^{14,§} A. Khoukaz,⁵ A. Khreptak,³ D.A. Kirillov,¹⁹ S. Kistryn,³ H. Kleines,^{14,§} B. Kłos,^{20,¶} W. Krzemień,⁶ P. Kulesa,¹⁰ A. Kupść,^{1,6} K. Lalwani,²¹ D. Lersch,^{13,**} B. Lorentz,^{13,*} A. Magiera,³ R. Maier,¹³ P. Marciniwski,¹ B. Mariański,^{2,‡} H.-P. Morsch,² P. Moskal,³ W. Parol,¹⁰ E. Perez del Rio,³ N.M. Piskunov,¹⁹ D. Prasuhn,¹³ D. Pszczel,^{1,6} K. Pysz,¹⁰ J. Ritman,^{13,22,*} A. Roy,¹⁸ O. Rundel,³ S. Sawant,²³ S. Schadmand,^{13,*} T. Sefzick,^{13,*} V. Serdyuk,¹³ B. Shwartz,⁷ T. Skorodko,^{11,12} M. Skurzok,^{3,††} J. Smyrski,³ V. Sopov,^{16,‡} R. Stassen,¹³ J. Stepaniak,⁶ E. Stephan,²⁰ G. Sterzenbach,¹³ H. Stockhorst,¹³ H. Ströher,¹³ A. Szczurek,¹⁰ A. Trzciński,^{2,‡} M. Wolke,¹ A. Wrońska,³ P. Wüstner,¹⁴ A. Yamamoto,²⁴ J. Zabierowski,²⁵ M.J. Zieliński,³ J. Złomańczuk,¹ P. Żuprański,² and M. Żurek²⁶
(WASA-at-COSY Collaboration)^{‡‡}

A. Deltuva,²⁷ J. Golak,³ A. Kozela,¹⁰ A. Łobejko,²⁸ P. U. Sauer,²⁹
R. Skibiński,³ I. Skwira-Chalot,³⁰ A. Wilczek,²⁰ and H. Witała³

- ¹Division of Nuclear Physics, Department of Physics and Astronomy, Uppsala University, Box 516, 75120 Uppsala, Sweden
²Nuclear Physics Division, National Centre for Nuclear Research, ul. Pasteura 7, 02-093, Warsaw, Poland
³M. Smoluchowski Institute of Physics, Jagiellonian University, prof. Stanisława Łojasiewicza 11, 30-348 Kraków, Poland
⁴School of Physics Engineering and Technology, The University of York, Heslington, York, YO10 5DD, UK
⁵Institut für Kernphysik, Westfälische Wilhelms-Universität Münster, Wilhelm-Klemm-Str. 9, 48149 Münster, Germany
⁶High Energy Physics Division, National Centre for Nuclear Research, ul. Pasteura 7, 02-093, Warsaw, Poland
⁷Budker Institute of Nuclear Physics of SB RAS, 11 Acad. Lavrentieva Pr., Novosibirsk, 630090 Russia
⁸Peter Grünberg Institut, PGI-6 Elektronische Eigenschaften, Forschungszentrum Jülich, 52425 Jülich, Germany
⁹Institut für Laser- und Plasmaphysik, Heinrich Heine Universität Düsseldorf, Universitätsstr. 1, 40225 Düsseldorf, Germany
¹⁰The Henryk Niewodniczański Institute of Nuclear Physics, Polish Academy of Sciences, ul. Radzikowskiego 152, 31-342 Kraków, Poland
¹¹Physikalisches Institut, Eberhard Karls Universität Tübingen, Auf der Morgenstelle 14, 72076 Tübingen, Germany
¹²Kepler Center for Astro and Particle Physics, Physikalisches Institut der Universität Tübingen, Auf der Morgenstelle 14, 72076 Tübingen, Germany
¹³Institut für Kernphysik, Forschungszentrum Jülich, 52425 Jülich, Germany
¹⁴Zentralinstitut für Engineering, Elektronik und Analytik, Forschungszentrum Jülich, 52425 Jülich, Germany
¹⁵Physikalisches Institut, Friedrich-Alexander Universität Erlangen-Nürnberg, Erwin-Rommel-Str. 1, 91058 Erlangen, Germany
¹⁶National Research Centre "Kurchatov Institute", Moscow, 123182 Russia
¹⁷II. Physikalisches Institut, Justus-Liebig-Universität Gießen, Heinrich-Buff-Ring 16, 35392 Giessen, Germany
¹⁸Discipline of Physics, Indian Institute of Technology Indore, Khandwa Road, Indore, Madhya Pradesh 453 552, India
¹⁹Veksler and Baldin Laboratory of High Energy Physics, Joint Institute for Nuclear Physics, 6 Joliot-Curie, Dubna, 141980 Russia
²⁰August Chelkowski Institute of Physics, University of Silesia, ul. 75 Pułku Piechoty 1, 41-500 Chorzów, Poland
²¹Department of Physics, Malaviya National Institute of Technology Jaipur, JLN Marg, Jaipur, Rajasthan 302 017, India
²²Institut für Experimentalphysik I, Ruhr-Universität Bochum, Universitätsstr. 150, 44780 Bochum, Germany
²³Department of Physics, Indian Institute of Technology Bombay, Powai, Mumbai, Maharashtra 400 076, India
²⁴High Energy Accelerator Research Organisation KEK, Tsukuba, Ibaraki 305-0801, Japan
²⁵Astrophysics Division, National Centre for Nuclear Research, Box 447, 90-950 Łódź, Poland
²⁶Physics Division, Argonne National Laboratory, 9700 S Cass Ave, Lemont, IL 60439, USA
²⁷Institute of Theoretical Physics and Astronomy, Vilnius University, Saulėtekio al. 3, LT-10257 Vilnius, Lithuania
²⁸Institute of Experimental Physics, Faculty of Mathematics, Physics and Informatics, University of Gdańsk, PL-80308 Gdańsk, Poland
²⁹Institute for Theoretical Physics, Leibniz University Hannover, D-30167 Hannover, Germany
³⁰Faculty of Physics, University of Warsaw, PL-02093 Warszawa, Poland

(Dated: December 30, 2025)

The differential cross section for the ${}^1\text{H}(d,pp)n$ breakup reaction at deuteron beam energy of 380 MeV has been determined with high precision for 189 angular configurations of outgoing protons in the region of forward laboratory angles. The cross section data were compared to theoretical predictions based on the state-of-the-art nucleon-nucleon potentials, combined with a three-nucleon

force, the Coulomb interaction or carried out in a relativistic approach. In the region of the lowest differential cross section, the discrepancy between the data and the theoretical predictions is observed, also in the case of relativistic calculations.

I. INTRODUCTION

Properties of nuclei at medium energies are determined to a large extent by pairwise nucleon-nucleon (NN) interactions, which are a dominant component of the nuclear potential. However, neglecting internal degrees of freedom of interacting nucleons, it is necessary to introduce the many-body forces, in particular the three-nucleon force (3NF). State-of-the-art models of 3NF's, like TM99 [1], Urbana IX [2], or Illinois [3], combined with the realistic nucleon-nucleon (2N) potentials, constitute the basis for calculations of binding energies and scattering observables. Chiral Effective Field Theory (ChEFT) provides a systematic construction of nuclear forces in a fully consistent way: the 3N forces appear naturally at a certain order [4, 5]. The theoretical calculations including semi-phenomenological 3NF or 3NF stemming from ChEFT, reproduce with high accuracy binding energies of light nuclei, see Refs. [6–8] and references therein.

A comprehensive description of nuclear forces requires an accurate understanding of the few-nucleon system dynamics. In particular, the three-nucleon system is the simplest one to test the interaction models and constrain the 3NF parameters. It was demonstrated that by including 3NF the description of differential cross section for elastic nucleon-deuteron scattering is significantly improved as compared to the calculations based on NN interactions only [9–11]. The remaining discrepancy between the data and theoretical calculations appears above 100 MeV/nucleon and has not been explained by either the influence of Coulomb interactions or relativistic effects, both of which are predicted to be small and very local. Studies of the $^1\text{H}(d, pp)n$ and $^2\text{H}(p, pp)n$ breakup reactions make important contribution to investigations of the 3NF. The advantage relies on the kinematic richness of the three-body final state. There are experimental evidences of significant 3NF contributions to the differential

cross section for the breakup reaction, starting already at relatively low beam energy of 65 MeV/nucleon [12, 13]. In contrast to the elastic scattering case, Coulomb interaction is a very important component of the breakup reaction dynamics. The Coulomb interaction between protons modifies the cross section data over a significant part of the phase space, in particular at forward laboratory angles of the $^1\text{H}(d, pp)n$ reaction [14–16]. At present, the Coulomb interaction and 3N forces are both included into theoretical calculations and their interplay can be studied [17–19].

The relativistic calculations of the differential cross section for breakup reaction led to different results than the non-relativistic ones [20]. Due to the predicted significant 3NF effects and relativistic effects in the energy region between 150 and 200 MeV/nucleon [20, 21], the question arises about their interplay. So far, no calculations have been performed that treat in fully relativistic way both the NN and 3NF interactions. Under such circumstances one has to rely on systematic (in beam energy) studies over large phase space regions, with the aim to single out both contributions on the basis of their different kinematic dependencies.

The very limited experimental data set in this range, especially when it comes to data covering wide ranges of phase space, became the motivation for the experiments described here. The exception, a measurement of the $^2\text{H}(p, pp)n$ at 190 MeV [22–24], provided hints for deficiencies in the description of the cross section for the deuteron breakup reaction, even when 3NF is included. The problem can be interpreted either as confirmation of the above mentioned issues in elastic scattering, or as a consequence of relativistic effects. Data presented in this work were taken in the inverse kinematics, $^1\text{H}(d, pp)n$, complementing the studied region of the reaction phase space. They were part of a systematic study conducted with the WASA detector at COSY beam in the energy range from 150 to 200 MeV/nucleon, from which data at 170 MeV/nucleon have been published so far [25].

II. EXPERIMENT AND DATA ANALYSIS

An experiment to investigate the $^1\text{H}(d, pp)n$ breakup reaction using a deuteron beam of 150, 170, 190, 200 MeV/nucleon was performed in January 2013 at the Cooler Synchrotron COSY-Jülich. Energies 170, 190 and 200 MeV/nucleon of the deuteron beam were changed in a supercycle mode of time length 30 s, while measurement at 150 MeV/nucleon was performed separately. Due to close to 4π acceptance and moderate detection threshold of the WASA (Wide Angle Shower Apparatus) detection system, differential cross section data have been collected in a large part of the breakup reaction phase space. In

* present address: GSI Helmholtzzentrum für Schwerionenforschung GmbH, Planckstraße 1, 64291 Darmstadt, Germany

† present address: Institut für Kernphysik, Johannes Gutenberg Universität Mainz, Johann-Joachim-Becher Weg 45, 55128 Mainz, Germany

‡ deceased

§ present address: Jülich Centre for Neutron Science JCNS, Forschungszentrum Jülich, 52428 Jülich, Germany

¶ Corresponding author: barbara.klos@us.edu.pl

** present address: Department of Physics, Florida State University, 77 Chieftan Way, Tallahassee, FL 32306-4350, USA

†† present address: INFN, Laboratori Nazionali di Frascati, Via E. Fermi, 40, 00044 Frascati (Roma), Italy

‡‡ the author list reflects the once-existing composition of the WASA-at-COSY Collaboration, within which the data presented in this paper have been obtained

this paper, the results of an analysis of the data collected at the beam energy of 190 MeV/nucleon are shown, with focus on the proton-proton coincidences registered in the Forward Detector.

A. WASA detector

The WASA detector [26, 27] (see Fig. 1) consisted of four main components: Central Detector (CD), Forward Detector (FD), Pellet Target and Scattering Chamber. The pellet target provided a narrow stream of frozen hydrogen droplets. The Central Detector operated in the experiment described here, but the present data analysis is limited to the registration of protons and deuterons only in the Forward Detector.

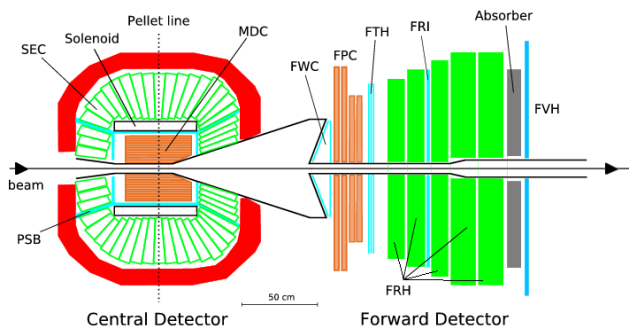


FIG. 1. (Color online) Schematic view of the detection system.

FD consisted of a set of detectors for the identification of charged hadrons and track reconstruction: Forward Window Counter (FWC), Forward Proportional Chamber (FPC) and plastic scintillators: Forward Trigger Hodoscope (FTH), Forward Range Hodoscope (FRH) and Forward Veto Hodoscope (FVH). FPC was used for precise determination of particle emission angles. The FD plastic scintillators were used for particle identification and particle energy measurement. They all provided information for the first-level trigger logic; for details see Ref. [25]. Between the second (FRH2) and third (FRH3) layers of FRH there were two layers of Forward Range Interleaving Hodoscope (FRI). In addition, between the layers FRH3 and FRH4, a passive aluminum layer was placed to extend the energy range of particles stopped in the WASA detector not shown in Fig. 1).

B. Data analysis

The data analysis presented in this work was focused on proton-proton coincidences from the $^1\text{H}(d, pp)n$ breakup reaction at 190 MeV/nucleon, registered in the Forward Detector. This was a follow-up of the analysis performed for data collected at 170 MeV/nucleon, described in detail in Ref. [25], thus the data analysis pro-

cedures were similar. Below we will present the main steps and focus on describing the differences associated with the different range of energies of particles in the exit channel. The multilayer structure of the Forward detector had a significant impact on the analysis procedures: as the energy of the outgoing particles increased, more layers were involved in the track reconstruction, which affected both energy calibration and detection efficiency.

In the first step of analysis, events of interest were selected: two protons from the breakup process and deuterons from elastic scattering channel, the latter used for the cross section normalization. The particle identification was based on the ΔE - E_R technique, where E_R was the remaining energy deposit in the layer where the particle was stopped and ΔE denoted the energy deposit in the preceding layer. In the entire range of energies, a clear separation between loci of protons and deuterons was observed, see examples in Fig. 2.

1. Analysis of breakup events

The breakup configuration was defined by the emission angles of the two outgoing protons: two polar angles θ_1 and θ_2 (with $\theta_1 \leq \theta_2$), between 5 and 15°, and their relative azimuthal angle φ_{12} . The data were integrated over the angular ranges of $\theta_{1,2} (\pm 1^\circ)$ and $\varphi_{12} (\pm 5^\circ)$. In order to reduce the background, cut on neutron peak in the missing mass spectrum [28] was applied. For each angular configuration, the data were placed in a kinematic spectrum showing the energy correlation of the proton pair, E_1 vs E_2 (see Fig. 3), and then transformed to the variable S , which shows the position along the kinematical curve [25]. The starting point of the S -curve ($S = 0$) is chosen as a point for which energy of the second proton is minimal. This step required precise energy calibration, which was based on measurements of dp elastic scattering at energies corresponding to minimum ionization [29]. Since the FRI detector was not used in a number of previous runs, its calibration was not included in the main calibration procedure and was known with lower accuracy. The appropriate corrections have been applied on the basis of energy deposited in the previous layer but the energy resolution was diminished. The affected energy region corresponded to the slope of the cross section S -distribution [28] and the solution was to apply adequately wide binning in S of 24 MeV. A similar issue arose for particles stopped in the aluminum layer between FRH3 and FRH4, and its impact on the reconstructed energy was even more pronounced due to the considerable thickness of this passive layer. Since it affected only the tails of the S -distributions, it was decided to discard these regions, which only slightly limited an S range of the cross section data.

The energy calibration was validated by the correlation of proton energies in each of the studied breakup configurations (see example in Fig. 3) and by reproduction of the neutron missing mass, for details see Ref. [28].

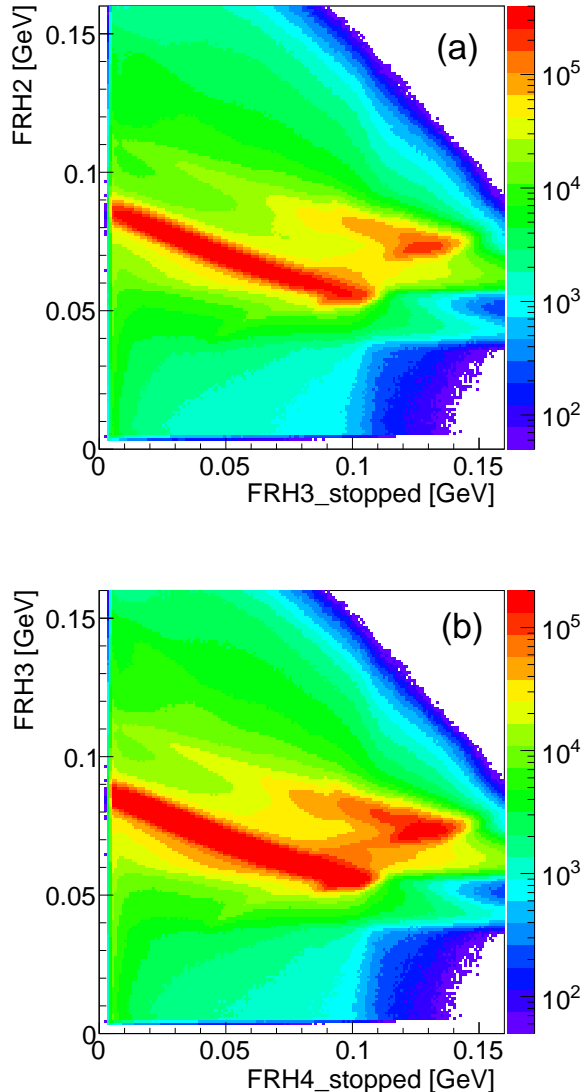


FIG. 2. Particle identification spectra of particles stopped in (a) 3rd layer and (b) 4th layer of FRH. Loci of protons and deuterons are clearly visible.

WASA Monte Carlo program based on the Geant 3 simulation package was used for precise determination of efficiency of the detection system. The analysis of generated data included the detector acceptance and all cuts applied in the analysis. The efficiency for registering and identifying elastically scattered deuterons was determined for each polar angle and typically reached about 80%. The efficiency for proton-proton coincidences was determined for each kinematical configuration with defined integration limits: $\Delta\theta_1=\Delta\theta_2=2^\circ$ and $\Delta\varphi_{12}=10^\circ$. Differently from the analysis performed at lower beam energy [25], a common efficiency factor did not apply for the entire S -range. This was due to the difference in the number of detector layers penetrated by coincident protons which depended on their energy. In the central

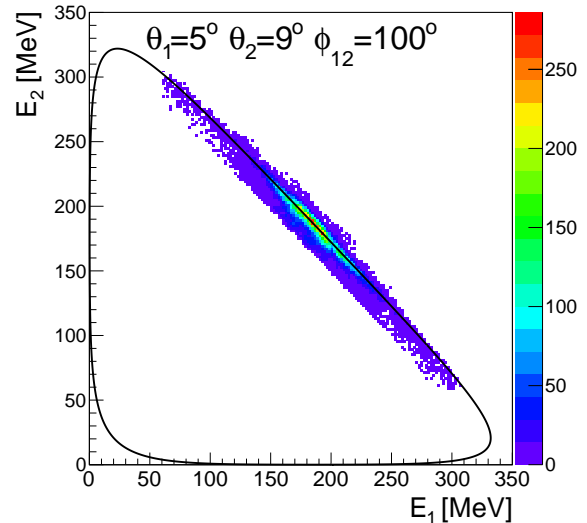


FIG. 3. (Color online) E_1 vs. E_2 coincidence spectrum of the two protons registered at $\theta_1=5^\circ \pm 1^\circ$, $\theta_2=9^\circ \pm 1^\circ$, and $\varphi_{12}=100^\circ \pm 5^\circ$. The solid line shows a three-body kinematical curve, calculated for the central values of experimental angular ranges.

part of the S distribution, typical efficiency for registering breakup events was 60%, while on the tails, it was reduced down to 50% due to one proton penetrating to the FRH3 layer [28].

2. Luminosity

The absolute normalization was derived from the luminosity determined on the basis of the number of elastically scattered deuterons. Deuterons were sorted with respect to their laboratory scattering angles, between 8° and 14° in a step of 1° . To remove the tail associated with hadronic interactions, limits were set on the deuteron peak in the corresponding energy spectra. After correcting for efficiency, the resulting number of deuterons recorded at each angle was normalised based on the known elastic scattering cross section.

Due to the considerable scatter of existing experimental data in the intermediate energies, a previously used strategy of a fit to a wide range of beam energies [25] was pursued. In the current analysis we also used the fact, that the angular range of elastically scattered deuterons corresponds to $\theta_{CM}^p < 50^\circ$, which is a region of a so-called soft-scattering. In the elastic scattering, a part of the momentum and energy is transferred from the beam to the target, thus the square of the four-momentum transfer $t < 0$, and it can be described by:

$$t = -2p^{*2}c^2(1 - \cos\theta_{CM}), \quad (1)$$

with p^* corresponding to the momentum and θ_{CM} denoting the beam particle scattering angle in the center

of mass system. A four-momentum transfer defined as $qc = \sqrt{-t}$ is related to the momentum transferred to the target and reflects the “hardness” of the collision. The soft collisions mentioned above are long-range collisions characterized by small q . This region is also called the *scaling region* and it is dominated by the direct term in the two-nucleon potential. Moreover, the dynamical part (after removing the phase-space factor) of the cross section predominately depends on the momentum transfer and has a very small dependence on the beam energy (for further discussion see Ref. [30]). The cross section dependence on the momentum transfer has dominating exponential character. For beam energies ranging between 108 and 250 MeV and momentum transfers $q < 280$ MeV/c, the $\ln\sigma_{CDB+TM99}$ calculated with the CD-Bonn potential combined with the TM99 3NF reveal a linear dependence on q . At $\theta_{CM} > 45^\circ$ and $q > 300$ MeV/c small departure from linearity can be observed. This validates the linear fit to the experimental data, with the exception of the highest q 's. In Fig. 4, the available pd elastic cross data and the corresponding fits are shown for two deuteron scattering angles.

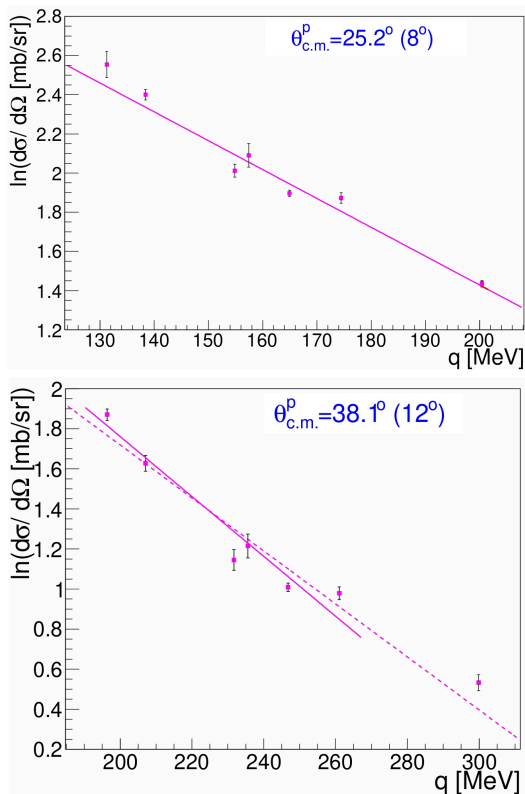


FIG. 4. (Color online) Experimental differential cross section of the deuteron-proton elastic scattering at the incident-beam energies: 108 MeV, 120 MeV, 150 MeV, 170 MeV, 190 MeV [31, 32], 155 MeV [33] and 250 MeV [10] presented as $\ln(\sigma)$ in a function of q for two scattering angles, specified in the panels. Two lines in the lower panel show linear fits including (dashed line) or excluding (solid line) the point for the highest beam energy of 250 MeV.

Similarly to the previous analysis [25], the fit results were cross-checked with theoretical calculations. In the soft scattering region, the theoretical calculations including 3NF, for example CDB+ Δ or CDB+TM99 (see Sec. III) provide adequate description of the data. At the lowest q one should however take into account Coulomb interactions modifying the cross section. Therefore, two types of calculations were taken into account: the one including Coulomb, CDB+ Δ +C, applicable in the full range of studied scattering angles, and CDB+TM99, to be used in the range of laboratory angles between 12° and 14° where the predicted Coulomb effects are below 2% (as stems from the comparison of the CDB+ Δ +C and CDB+ Δ predictions). The calculated cross section values were used for determining integrated luminosity. The corresponding data points (cyan triangles and magenta dots in Fig. 5) have uncertainties resulting from uncertainties of the detection efficiency corrections. These results are compared to the luminosity values (blue stars) obtained with the experimental cross sections resulting from the fits described above. In the latter case, uncertainties of the $\ln\sigma$ vs. q fits were included in the final uncertainty boxes. The spread of results within each of the methods illustrates differences of shapes of angular cross section distributions obtained in this experiment and the corresponding normalization cross sections.

This spread sometimes exceeds the estimated systematic uncertainties of individual points. For each normalization method, the corresponding average was calculated, with weights that include systematic uncertainties (horizontal lines, as specified in the legend of Fig. 5). Analogous to the previous analysis [25], the result obtained with CDB+TM99 potential is taken as a luminosity value (horizontal solid magenta line in Fig. 5), and the other ones are used to determine systematic uncertainty. The systematic uncertainties marked as horizontal black dashed lines cover the range of scatter of individual data points obtained with all three normalization methods. Finally, the average integrated luminosity obtained for the full set of data is $(3.036 \pm 0.003) \cdot 10^7 \text{ mb}^{-1}$ with asymmetric systematic uncertainty of $(-0.254, +0.093) \cdot 10^7 \text{ mb}^{-1}$, corresponding to a relative error of -8% and +3%.

3. Experimental uncertainties

Statistical uncertainties of the measured cross-section values comprise an uncertainty of the measured number of the breakup coincidences and of the luminosity. In all 189 kinematic configurations statistical errors in peaks of the cross-section distributions are below 1%.

The data consistency checks and discussion of systematic uncertainties presented in Ref. [25] are valid also for the data set presented here. The systematic uncertainties dominate over statistical ones and stem primarily from three sources:

- Luminosity determination, which affects the com-

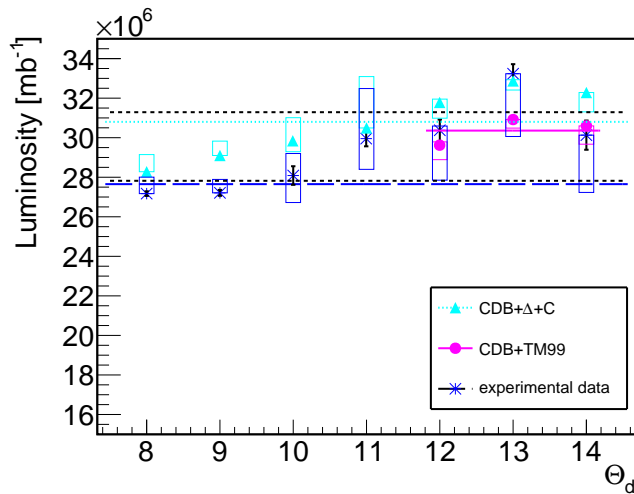


FIG. 5. (Color online) Determination of the integrated luminosity. The integrated luminosity values were calculated independently for each deuteron scattering angle. Each set of points and corresponding average (horizontal line) corresponds to a different way of determining elastic scattering cross section used for normalization, as specified in the legend. Two additional dashed lines present the systematic uncertainty of the final result. For more details see the text.

mon normalization factor for all data points. The systematic uncertainty of the luminosity, as discussed in Sec. II B 2, is asymmetric and leads to uncertainty of the cross section: -3% and $+8\%$.

- Uncertainty of efficiency for detecting proton-proton coincidences. It corresponds to the accuracy of the MC simulations and consists of two parts: the systematic error of hadronic interaction modeling (7%) and the statistical accuracy of the simulations; the latter one varies typically between 1% and 7% (only in 6 out of 189 configurations it exceeds 7%).
- Background subtraction procedure - the corresponding uncertainty was determined for each data point in two ways: varying the range around the gaussian peak where the linear background was determined, and checking gaussian shape of the distribution obtained after the background subtraction (by comparing the integral of the fitted Gauss with the sum of events); in the central parts of the S -distributions it varies between 1 and 9%.

Finally, summing all the components in squares, we obtain systematic uncertainties ranging between 8 and 16% for the central regions of the studied S distributions, thus dominating over the statistical ones.

III. THEORETICAL CALCULATIONS

The experimental cross section data measured at 190 MeV/nucleon have been compared to results of the

same set of the calculations as in case of the earlier published data collected at 170 MeV/nucleon. The list of theoretical approaches is given in Table I, for details see Ref. [25] and references therein. To study the impact of individual contributions to the system dynamics, a comparison was first made with calculations based on pure NN potentials (2N and CDB in Table I). Next, the 3NF was taken into account (2N+TM99, CDB+ Δ). The Coulomb interaction was applied to a purely nucleonic CDB potential (CDB+C) and its coupled-channel extension (CDB+ Δ +C). In one case, CDBrel, the relativistic effects were taken into account. The group of calculations, CDB, CDB+TM99, 2N, 2N+TM99, CDBrel, was performed by Witała et al., while the second group, CDB, CDB+ Δ and CDB+ Δ +C, was performed by Deltuva.

Prior to comparing with the data, the theoretical predictions were averaged over the same angular bins as used in the data analysis ($\Delta\theta_{1,2} = 2^\circ$, $\Delta\varphi_{12} = 10^\circ$) and projected onto relativistic kinematics, see Ref. [13]. The relativistic calculations are the only exception: the calculations were performed for central values of the angular ranges alone.

TABLE I. Definition of abbreviations applied for naming theoretical calculations. “aver” means averaging over angular ranges accepted in data analysis.

abbreviation	description	aver	Ref.
CDB	CD Bonn potential	Yes	[34, 35]
CDB+TM99	CD Bonn potential combined with TM99 3NF	Yes	[1, 36, 37]
2N	potentials: AV18, CD Bonn, Nijmegen I and II	Yes	[34, 35, 38, 39]
2N+TM99	potentials (as above) combined with TM99 3NF	Yes	[1, 36, 37]
CDB+ Δ	coupled-channel potential CD Bonn+explicit Δ	Yes	[40]
CDB+ Δ +C	coupled-channel potential CDB+ Δ with Coulomb force	Yes	[17, 18]
CDBrel	CD Bonn potential relativistic calculations	No	[21]

The most extensive developments of nuclear potentials are nowadays carried out within the framework of ChEFT. It has been shown, that with regard to NN interactions it is necessary to perform calculations at 5th order ($\nu=5$), *i.e.* N4LO (see the discussion in [5]). Thus, the 3NF at the same order is required for the consistency. So far the complete calculations for Nd system at N3LO

are unavailable and only approaches based on the realistic potentials are considered in this work. Recent developments in calculating observables for the breakup reaction within ChEFT approach are discussed in Ref. [8].

IV. RESULTS

The differential cross section for a regular grid of polar and azimuthal angles with a constant step in arclength variable S (24 MeV) was experimentally obtained. Polar angles of the two protons, θ_1 and θ_2 , were changed between 5° and 15° with the step size of 2° and their relative azimuthal angle φ_{12} was analyzed in the range from 20° to 180° , with the step size of 20° . In total, 189 configurations have been analysed. Fig. 6 presents cross section distributions for the configurations for which relativistic calculations are available.

This set can be considered representative for the studied phase space, with the smallest (5°) and largest (15°) among the analyzed polar angles, both symmetric and maximally asymmetric cases (respectively $\theta_2 - \theta_1 = 0^\circ$ and 10°), combined with two very different relative azimuthal angles ($\varphi_{12} = 60^\circ$ and 180°). The data are compared to all the theoretical calculations listed in Table I. Theoretical bands correspond to non-relativistic 2N and 2N+TM99 calculations by Witała et al. and their width is related to differences between predictions obtained with individual NN potentials. Since the bands are narrow, further in quantitative analyses only CDB and CDB+TM99 will be used. In all the cases shown in Fig. 6, relativistic calculations are significantly below the data. The predicted 3NF effects are small or negligible. In the top panels, a certain underestimation of the measured cross section by theories is observed, but roughly contained within systematic uncertainties. This statement requires quantitative verification. In one case the Coulomb effect is clearly present. The configurations shown in the bottom panels, with $\theta_1 = \theta_2 = 15^\circ$, are characterized by a very low cross section, one or two orders lower (in the peaks) than maximal cross section values in the top panels. In these cases all the calculations significantly underestimate the experimental data. This confirms the findings from the measurement at 170 MeV/nucleon [25], though for the discussed currently data at 190 MeV/nucleon, discrepancies are even more pronounced, reaching a factor of 2 in the best case, or even 4 in the case of the relativistic approach.

Figs. 11 - 21 in Appendix A present the differential cross section results for the full set of studied kinematic configurations. A brief review of them leads to similar qualitative conclusions:

- 3NF effects are small in the entire angular region under study.

- Coulomb effects, as expected, dominate in the most forward configurations ($\theta_1, \theta_2 = 5^\circ$ or 7°) with the lowest ($\varphi_{12} = 20^\circ$) and highest ($\varphi_{12} \geq 140^\circ$) relative azimuthal angles. In these regions the calculations including Coulomb interaction provide more adequate results than other ones, though in some cases the Coulomb effect is less pronounced in the data than predicted by theory.
- The overall description of the data for configurations with $\varphi_{12} \leq 100^\circ$ is good, and while the experimental points lie systematically above the theoretical lines, the differences are comparable to systematic uncertainties and may be due to uncertainty of the luminosity.
- In configurations with the largest studied polar angles ($\theta_1 = \theta_2 = 13^\circ, 15^\circ$), nearly coplanar ($\varphi_{12} = 160^\circ, 180^\circ$), the theoretical predictions deviate very strongly from the data, underestimating them.

These observations will be further quantitatively discussed by means of a χ^2 analysis.

A. χ^2 analysis

Quantitative analysis of the description of the cross section data (σ_{exp}) provided by various calculations (σ_{teor}) is performed in terms of χ^2 -like variables. Due to the dominating contribution of systematic uncertainties, the following definition has been applied, which also facilitates direct comparisons with the results from Ref. [25]:

$$\chi^2 = \frac{1}{n_{d.o.f.}} \sum \frac{(\sigma_{teor}(\xi) - \sigma_{exp}(\xi))^2}{(\Delta\sigma_{st}(\xi) + \Delta\sigma_{sys}(\xi))^2}, \quad (2)$$

where ξ represents a set of kinematic variables $\xi=(\theta_1, \theta_2, \varphi_{12}, S)$, $\Delta\sigma_{st}(\xi)$ and $\Delta\sigma_{sys}(\xi)$ denote statistical and systematic uncertainties, respectively, summing goes over certain set of kinematic variables and $n_{d.o.f.}$ is a number of data points included in this sum. The quantity defined in this way has no precise statistical meaning, but it still provides a measure of the description provided by different models and allows comparison of possible deviations with experimental uncertainties.

The χ^2 per degree of freedom defined above has been calculated globally, individually for the kinematic configurations and, in addition, for the data sorted according to combination of polar angles θ_1, θ_2 or a relative azimuthal angle φ_{12} of the two protons. The global analysis (see Fig. 7) indicates that the quality of the description of the data is worse than for the data at 170 MeV/nucleon energy, where analogously defined χ^2 values covered the range between 3 and 7 [25]. Current values obtained at the beam energy of 190 MeV/nucleon are roughly 3 times higher, which is surprising given the small difference in beam energies and the same angular range in the laboratory system, thus a very similar phase space. Global

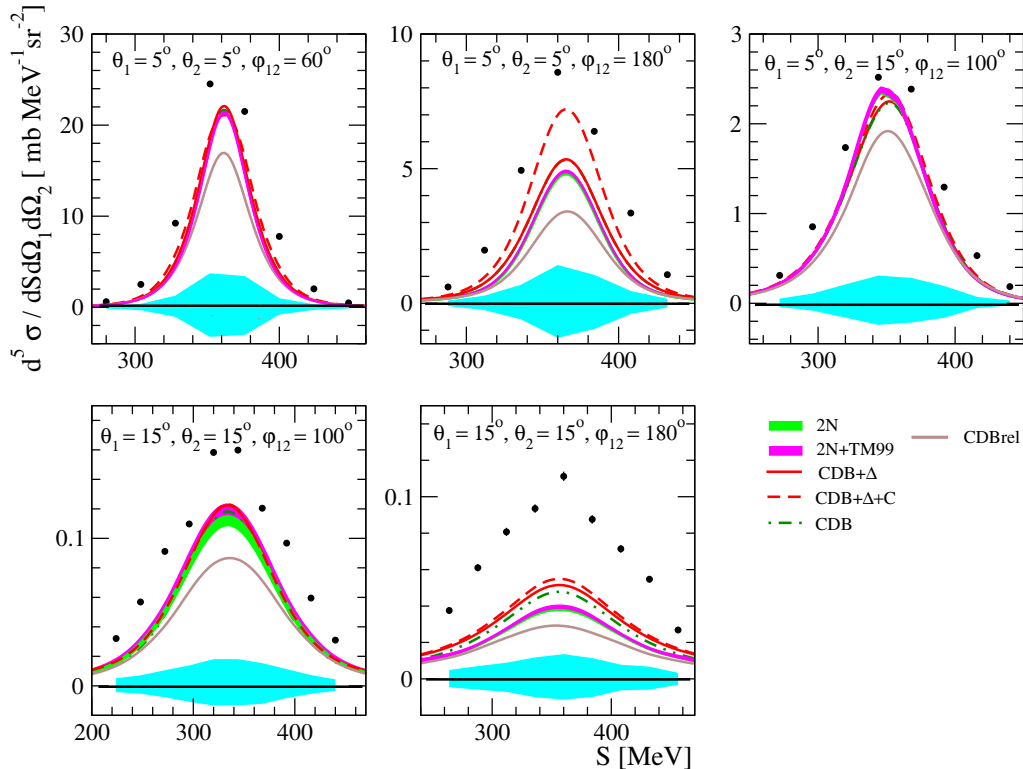


FIG. 6. (Color online) Differential cross section of ${}^1\text{H}(d, pp)n$ breakup reaction at beam energy of 190 MeV/nucleon shown in a function of the S variable for the set of configurations specified in the panels. Bars representing statistical uncertainties are usually smaller than data points. Systematic uncertainties are represented by bands. Data are compared to theoretical calculations specified in the legend.

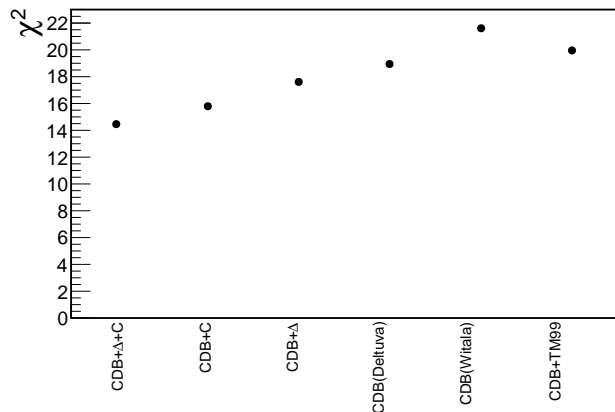


FIG. 7. (Color online) Quality of description of the differential cross section for the breakup reaction at 190 MeV/nucleon beam energy at forward angles. The global $\chi^2/d.o.f.$ (systematic errors included) was obtained as a result of comparing the cross section data with each of six types of theoretical calculations specified on the axis.

analysis indicates an improvement in description due to the inclusion of Coulomb interaction or of 3NF (TM99 force or explicit Δ isobar approach), with the best result

achieved when both contributions are included. However, the aforementioned effects are small compared to the global imperfection of the description.

In order to ascertain whether the deterioration of the description occurs in the entire phase space studied in the experiment, and to look for areas sensitive to individual contributors to the dynamics, the quality of description was studied in a function of kinematic variables. Dependence of χ^2 on φ_{12} angle was examined first. The analysis (see Fig. 8(a)) clearly indicates the region of dominance of the Coulomb effect at the largest relative azimuthal angles. Surprisingly, the improvement of description related to introducing Coulomb interactions is not so obvious in the region of the lowest φ_{12} , close to proton-proton FSI. Calculations predict there strong sensitivity to Coulomb interaction, which lowers cross section, but in certain configurations data lie just between calculations with and without Coulomb interaction (see for example a configuration of $\theta_1=5^\circ$, $\theta_2=5^\circ$, $\varphi_{12}=20^\circ$ in Fig. 11), resulting in similar χ^2 's for both cases.

Already at the beam energy of 170 MeV/nucleon, significant difference of shapes (widths) of cross section distributions was observed: experimental S distributions were wider than theoretical ones [25]. This effect might

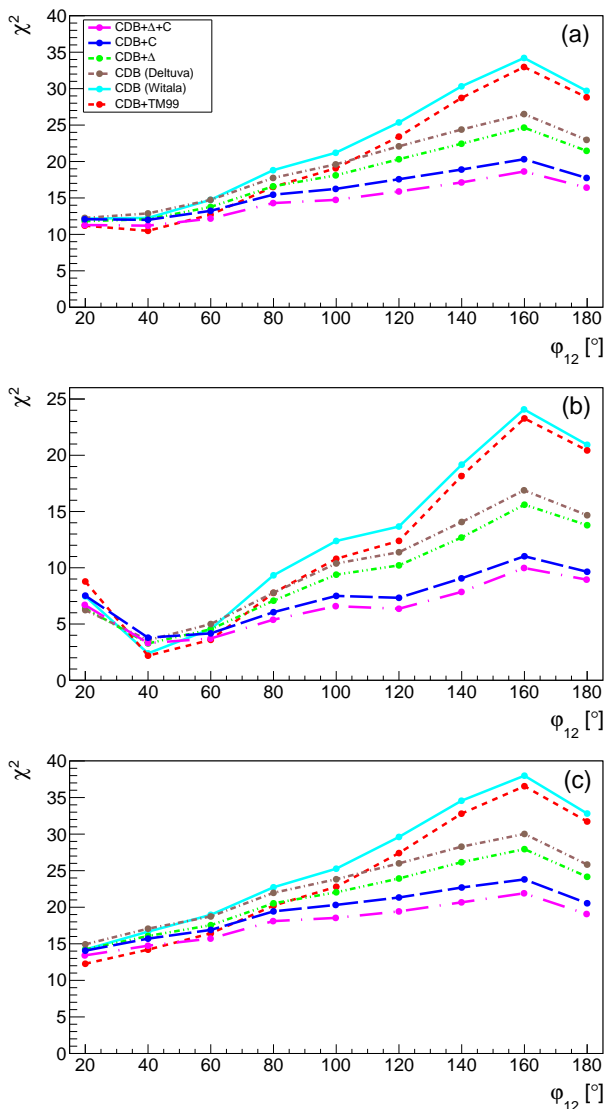


FIG. 8. (Color online) The $\chi^2/d.o.f.$ calculated for set of data characterised with given relative azimuthal angle ϕ_{12} : (a) whole S -distributions were taken into account; (b) only central parts of S -distributions were taken into account; (c) only tails of S -distributions were taken into account.

be partially attributed to relativistic effects in kinematics, but it persists even for relativistic calculations. In the data set presented here, experimental distributions are about 12-14% wider than theoretical ones, while variations of widths within theoretical calculations are on the level of 4%. To examine impact of the difference of shapes on the quality of the data description, the above presented analysis of χ^2 in a function of φ_{12} was repeated separately for two data subsets: data points lying in the central part of each kinematics (maximum of the cross section distribution) and data belonging to the tails of the distributions, see respectively Fig. 8(b) and (c). The general trends are similar, but in the case of CDB+ Δ +C calculations, χ^2 values are 2 or 3 times lower for peaks

than for tails. Also the contribution of tails to χ^2 is rather uniform, see Fig. 8(c), while for peaks (Fig. 8(b)), the quality of description in particular regions is more diverse. There is generally good description of data for φ_{12} of 40° and 60°, where the sensitivity to the interaction dynamics included in calculations is low. The Coulomb interaction has large impact at high φ_{12} . The 3NF effects, if present, practically vanish in integration over other kinematic variables.

The analysis of data sorted with respect to polar angles θ_1, θ_2 (Fig. 9) was carried out in two variables: difference $\theta_2 - \theta_1$ reflecting “asymmetry” of the configuration (individual panels in Fig. 9) and an average of the polar angles $(\theta_1 + \theta_2)/2$. Clearly, the Coulomb force dominates in the FSI region, characterised by the lowest difference of polar angles and the lowest average polar angles, between 5° and 7°. Moreover, description of the data improves with rising asymmetry of polar angles and/or for medium average of about 10°. The region of certain sensitivity to 3NF can be, in turn, identified at more symmetric configurations (three top panels) with high average $(\theta_1 + \theta_2)/2 \geq 13^\circ$, but this effect is tiny.

The maps of χ^2 for individual configurations prepared for four theoretical calculations are shown in Fig. 10. For the purpose of this comparison, a set of theories has been chosen that allows the Coulomb and 3NF effects to be traced both separately and together. For better visibility of effects, the maximum of colour z-axis was artificially set to 25. In all the maps one can observe a kind of stepped pattern corresponding to the fact, that configurations more asymmetric in polar angles are better described by the theories. In the case of CDBonn potential alone, it is apparent that for $\varphi_{12} > 100^\circ$ (right hand side of the map) the agreement between data and theory is poor. Only small change of picture due to 3NF (CDB+ Δ) is observed, as was expected from the small size of these predicted effects. On the map corresponding to CDB+C calculations the improvement of description is clearly visible. Adding both Coulomb interaction and 3NF (CDB+ Δ +C) leads to further small improvement of description. In the region of large polar and azimuthal angles (top right corner of the map) a lot of room for improvement remains, as was expected from examining particular cross section distributions in Fig. 6.

V. SUMMARY

The measurement of differential cross section of the $^1\text{H}(d, pp)n$ reaction at three beam energies, 170, 190 and 200 MeV/nucleon, changed in a supercycle mode allowed good control over data consistency and experimental uncertainties, constituting the basis for systematic comparison of the results. In this work, the differential cross section for beam energy 190 MeV/nucleon is presented for 189 configurations characterized with forward proton emission angles in the laboratory system and compared to a set of theoretical calculations. In this re-

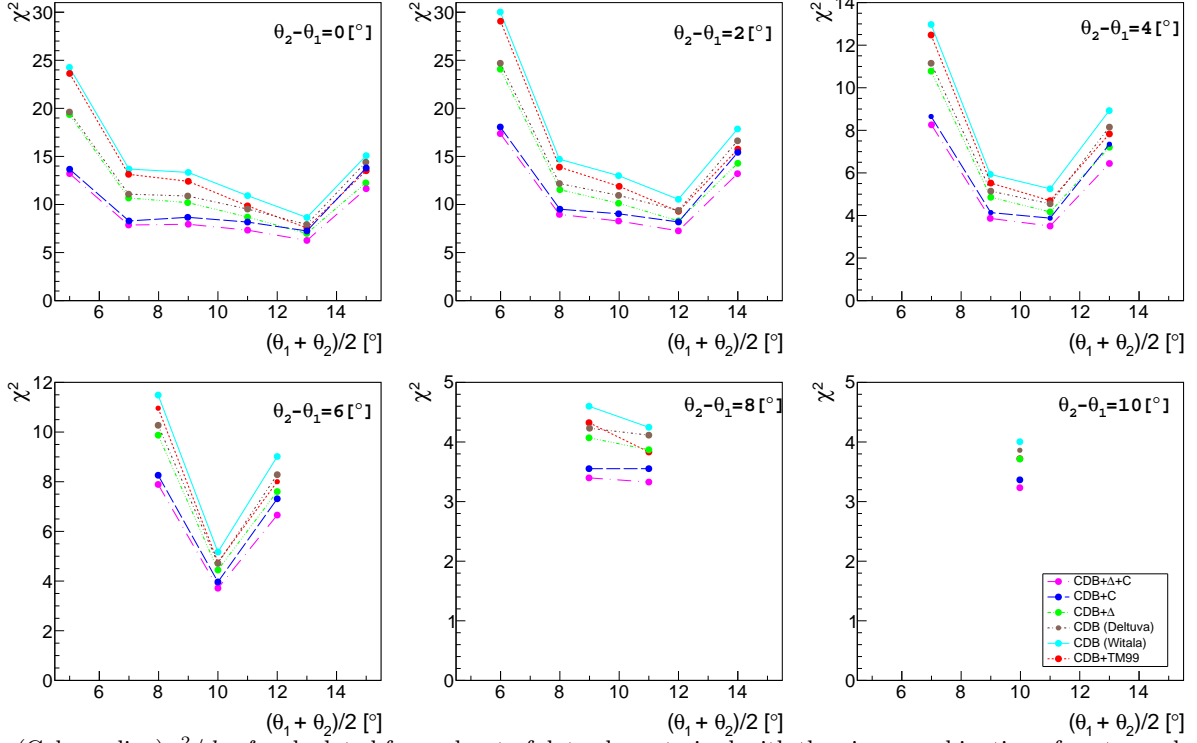


FIG. 9. (Color online) $\chi^2/d.o.f.$ calculated for each set of data characterised with the given combination of proton polar angles. The results are ordered according to difference of polar angles $\theta_{12} = \theta_1 - \theta_2$; in each panel results for one value of θ_{12} are shown.

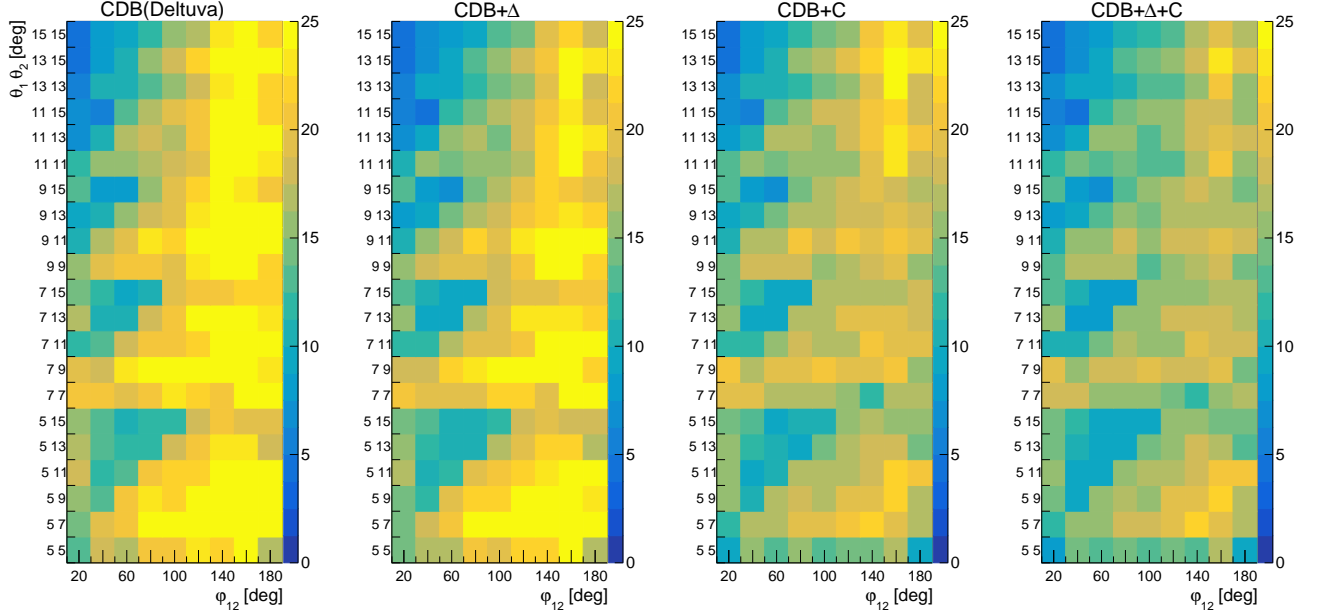


FIG. 10. (Color online) The $\chi^2/d.o.f.$ results obtained for all angular configurations separately, presented as the 2-dimensional map for selected theories, specified at the top of panels

gion, predicted 3NF effects are small, while calculated Coulomb effects are significant, especially at low polar angles of emitted protons. Relativistic calculations were performed for several selected configurations with CD-

Bonn potential alone, showing significant influence on the cross section compared to the same calculations in non-relativistic approach.

Confronting these prediction with the data, we clearly

confirm observation of the Coulomb effects, though in some cases calculations including Coulomb interactions underestimate the data. It is not clear, whether this can be attributed to relativistic effects or other missing dynamical effect. Moreover, general deterioration of the overall data description is observed, as compared to data collected at slightly lower beam energy of 170 MeV/nucleon. Most data lies above the theoretical predictions, but in many cases this difference is contained within systematic uncertainties, while the significant disagreements are observed in tails of the cross section S -distributions. This problem is related to different widths of the theoretical and experimental distributions. Apart of this issue, the description of data in the peaks is quite successful for majority of configurations, in particular after Coulomb interaction is included.

We have, however, localized a set of kinematical configurations of large disagreements between the experimental data and all the available theoretical calculations. This mainly concerns configurations with polar angles of $\theta_1 = \theta_2 = 13^\circ$ or 15° and coplanar or nearly coplanar geometries ($\varphi_{12} = 160^\circ, 180^\circ$), where the differential cross section is the lowest in the studied phase space. The discrepancies between data and theories roughly of the factor of 2 are observed. The latter finding is consistent with that followed from the previously analyzed cross section data at 170 MeV/nucleon. There, local underestimation of data with theories was observed for exactly the same configurations. Comparisons of these two data sets indicate the discrepancy rising with the beam energy. Calculations performed in the relativistic approach, limited to the CD-Bonn potential, further increase the discrepancy, leaving room for very large effects of the 3NF, well beyond the predictions of current models. This suggests either problem with currently available 3NF's at so high energy, or huge relativistic effects in the 3NF's.

Importantly, similar underestimation the data by theoretical predictions was observed in the cross section data collected at the same center of mass energy, but in the direct kinematics ${}^2\text{H}(p, pp)n$ [22–24]. There, the discrepancies were also observed locally, in symmetric configurations with $\varphi_{12} \geq 160^\circ$. In spite of these similarities, those configurations corresponded to a different θ_{CM} region. Also, in the regions of disagreements the predicted relativistic effects were small: either negligible, or shifting the results of calculations slightly towards the data, though far too small to solve the problem.

Systematic studies of the deuteron breakup in collision with proton at relatively high energies are important for testing current approaches to describe nuclear interactions. The differential cross section exhibits surprising sensitivity to missing elements of the dynamics, also in the regions where current 3NF models do not predict any

spectacular effects. Since relativistic calculations based on pure NN interaction show the effect opposite to the one needed for the correct data description, an approach that takes into account relativistic effects together with a full complexity of interaction potential, including 3NF, would be of great interest.

ACKNOWLEDGMENTS

This work was partly supported by the National Science Centre, Poland, under Grant No. IMPRESS-U 2024/06/Y/ST2/00135 and by the Excellence Initiative–Research University Program at the Jagiellonian University in Kraków. The numerical calculations were partly performed on the supercomputers of the JSC, Jülich, Germany. We thank the COSY crew for their work and the excellent conditions during the beam time.

Appendix A

Appendix A contains all the differential cross section distributions for the ${}^1\text{H}(d, pp)n$ breakup reaction at the beam energy of 190 MeV/nucleon obtained in the analysis described in this paper. Each set presents 9 configurations corresponding to individual azimuthal angles φ_{12} from 20° to 180° and one combination of θ_1 and θ_2 specified in the Figure. Since the 3NF effects are generally small and the results weakly depend on the model used, for clarity only calculations with one 2N potential (CD-Bonn) and one 3NF model (explicit treatment of Δ isobar) are shown.

- [1] S. A. Coon and H. K. Han, *Few-Body Syst.* **30**, 131 (2001).
- [2] B. S. Pudliner, V. R. Pandharipande, J. Carlson, S. C. Pieper, and R. B. Wiringa, *Phys. Rev. C* **56**, 1720 (1997).
- [3] S. C. Pieper, V. R. Pandharipande, R. B. Wiringa, and J. Carlson, *Phys. Rev. C* **64**, 014001 (2001).
- [4] E. Epelbaum, H.-W. Hammer, and U.-G. Meißner, *Rev. Mod. Phys.* **81**, 1773 (2009).
- [5] R. Machleidt and F. Sammarruca, *Physica Scripta* **91**, 083007 (2016).
- [6] J. Carlson, S. Gandolfi, F. Pederiva, S. C. Pieper, R. Schiavilla, K. E. Schmidt, and R. B. Wiringa, *Rev. Mod. Phys.* **87**, 1067 (2015).
- [7] M. Piarulli, A. Baroni, L. Girlanda, A. Kievsky, A. Lovato, E. Lusk, L. E. Marcucci, S. C. Pieper, R. Schiavilla, M. Viviani, and R. B. Wiringa, *Phys. Rev. Lett.* **129**, 052503 (2018).
- [8] P. Maris, R. Roth, E. Epelbaum, R. Furnstahl, J. Golak, K. Hebeler, T. Hübner, H. Kamada, H. Krebs, H. Le, U.-G. Meißner, J. Melendez, A. Nogga, P. Reinert, R. Skibiński, J. Vary, H. Witała, and T. Wolfgruber, *Phys. Rev. C* **106**, 064002 (2022).
- [9] H. Witała, W. Glöckle, D. Hüber, J. Golak, and H. Kamada, *Phys. Rev. Lett.* **81**, 1183 (1998).
- [10] K. Hatanaka, Y. Shimizu, D. Hirooka, J. Kamiya, Y. Kitamura, Y. Maeda, T. Noro, E. Obayashi, K. Sagara, T. Saito, H. Sakai, Y. Sakemi, K. Sekiguchi, A. Tamii, T. Wakasa, T. Yagita, K. Yako, H. P. Yoshida, H. K. V. P. Ladygin and, W. Glöckle, J. Golak, A. Nogga, and H. Witała, *Phys. Rev. C* **66**, 044002 (2002).
- [11] P. Mermod, J. Blomgren, B. Bergenwall, A. Hildebrand, C. Johansson, J. Klug, L. Nilsson, N. Olsson, M. Österlund, S. Pomp, U. Tippawana, O. Jonsson, A. Prokofiev, P.-U. Renberg, P. Nadel-Turonski, Y. Maeda, H. Sakai, and A. Tamii, *Phys. Lett. B* **597**, 243 (2004).
- [12] S. Kistryn, E. Stephan, A. Biegun, K. Bodek, A. Deltuva, E. Epelbaum, K. Ermisch, W. Glöckle, J. Golak, N. Kalantar-Nayestanaki, H. Kamada, M. Kiš, B. Kłos, A. Kozela, J. Kuroš-Żołnierczuk, M. Mahjour-Shafiei, U.-G. Meißner, A. Micherdzińska, A. Nogga, P. U. Sauer, R. Skibiński, R. Sworst, H. Witała, J. Zejma, and W. Zipper, *Phys. Rev. C* **72**, 044006 (2005).
- [13] S. Kistryn and E. Stephan, *J. Phys. G: Nucl. Part. Phys.* **40**, 063101 (2013).
- [14] S. Kistryn, E. Stephan, B. Kłos, A. Biegun, K. Bodek, I. Ciepał, A. Deltuva, A. Fonseca, N. Kalantar-Nayestanaki, M. Kiš, A. Kozela, M. Mahjour-Shafiei, A. Micherdzińska, P. Sauer, R. Sworst, J. Zejma, and W. Zipper, *Phys. Lett. B* **641**, 23 (2006).
- [15] I. Ciepał, B. Kłos, S. Kistryn, E. Stephan, A. Biegun, K. Bodek, A. Deltuva, E. Epelbaum, M. Eslami-Kalantari, A. C. Fonseca, J. Golak, N. Kalantar-Nayestanaki, H. Kamada, G. Khatri, D. Kirillov, D. Kirillov, S. Kliczewski, A. Kozela, M. Kravcikova, H. Machner, A. Magiera, G. Martinska, J. Messchendorp, A. Nogga, W. Parol, A. Ramazani-Moghaddam-Arani, B. J. Roy, H. Sakai, P. U. Sauer, K. Sekiguchi, I. Sitnik, R. Siudak, R. Skibiński, R. Sworst, J. Urban, H. Witała, and J. Zejma, *Few-Body Syst.* **56**, 665 (2015).
- [16] I. Skwira-Chalot, N. Kalantar-Nayestanaki, S. Kistryn, A. Kozela, and E. Stephan, *Few-Body Syst.* **65**, 10.1007/s00601-024-01892-7 (2024).
- [17] A. Deltuva, A. C. Fonseca, and P. U. Sauer, *Phys. Rev. C* **72**, 054004 (2005).
- [18] A. Deltuva, A. C. Fonseca, and P. U. Sauer, *Phys. Rev. C* **73**, 057001 (2006).
- [19] A. Deltuva, *Phys. Rev. C* **80**, 064002 (2009).
- [20] H. Witała, J. Golak, R. Skibiński, W. Glöckle, W. Polyzou, and H. Kamada, *Few-Body Syst.* **49**, 61 (2011).
- [21] R. Skibiński, H. Witała, and J. Golak, *Eur. Phys. J. A* **30**, 369 (2006).
- [22] H. Mardanpour, *Investigation of nuclear forces in $d+p$ elastic and $p+d$ break-up reactions at intermediate energies*, Ph.D. thesis, RUG (2008).
- [23] H. Mardanpour, H. R. Amir-Ahmadi, R. Benard, A. Biegun, M. Eslami-Kalantari, N. Kalantar-Nayestanaki, M. Kis, S. Kistryn, A. Kozela, H. Kuboki, Y. Maeda, M. Mahjour-Shafiei, J. G. Messchendorp, K. Miki, S. Noji, A. Ramazani-Moghaddam-Arani, H. Sakai, M. Sasano, K. Sekiguchi, E. Stephan, R. Sworst, Y. Takahashi, and K. Yako, *Few-Body Syst.* **44**, 49 (2008).
- [24] H. Tavakoli-Zaniani, M. Eslami-Kalantari, H. Amir-Ahmadi, M. Bayat, A. Deltuva, J. Golak, N. Kalantar-Nayestanaki, S. Kistryn, A. Kozela, H. Mardanpour, J. Messchendorp, M. M. Dadkan, A. Ramazani-Moghaddam-Arani, R. Ramazani-Sharifabadi, R. Skibiński, E. Stephan, and H. Witała, *Eur. Phys. J. A* **57**, 57 (2021).
- [25] P. Adlarson, W. Augustyniak, W. Bardan, M. Bashkanov, F. S. Bergmann, M. Berłowski, A. Bondar, M. Büscher, H. Calén, I. Ciepał, H. Clement, E. Czerwiński, K. Demmich, R. Engels, A. Erven, W. Erven, W. Eyrich, P. Fedorets, K. Föhl, K. Fransson, F. Goldenbaum, A. Goswami, K. Grigoryev, L. Heijkenkjöld, V. Hejny, N. Hüsen, L. Jarczyk, T. Johansson, B. Kamys, G. Kemmerling, A. Khoukaz, A. Khreptak, D. A. Kirillov, S. Kistryn, H. Kleines, B. Kłos, W. Krzemień, P. Kulessa, A. Kupś, K. Lalwani, D. Lersch, B. Lorentz, A. Magiera, R. Maier, P. Marciniowski, B. Mariański, H.-P. Morsch, P. Moskal, W. Parol, E. Perez del Rio, N. M. Piskunov, D. Prasuhn, D. Pszczel, K. Pysz, J. Ritman, A. Roy, O. Rundel, S. Sawant, S. Schadmand, T. Sefzick, V. Serdyuk, B. Shwartz, T. Skorodko, M. Skurzok, J. Smyrski, V. Sopot, R. Stassen, J. Stepaniak, E. Stephan, G. Sterzenbach, H. Stockhorst, H. Ströher, A. Szczurek, A. Trzciński, M. Wolke, A. Wrońska, P. Wüstner, A. Yamamoto, J. Zabierowski, M. J. Zieliński, J. Złomańczuk, P. Żuprański, M. Żurek, A. Deltuva, J. Golak, A. Kozela, R. Skibiński, I. Skwira-Chalot, A. Wilczek, and H. Witała (WASA-at-COSY Collaboration), *Phys. Rev. C* **101**, 044001 (2020).
- [26] C. Bargholtz, M. Bashkanov, M. Berłowski, A. Bondar, D. B. W. Brodowski, J. B. H. Calén, F. Capellaro, A. Chilingarov, H. Clement, J. Comfort, L. Demirors, C. Ekstrom, K. Fransson, C.-J. Fridén, L. Gerén, M. Gornov, V. Grebenev, J. Greiff, Y. Gurov, L. Gustafsson, B. Hoistad, G. Ivanov, M. Jacewicz, E. Jiganov, A. Johansson, T. Johansson, S. Keleta, O. Khakimova, A. Khoukaz, K. Kilian, N. Kimura, I. Koch, G. Kolachev, F. Kren, S. Kullander, A. Kupsc, A. Kuzmin,

- A. Kuznetsov, K. Lindberg, P. Marciniewski, R. Meier, O. Messner, B. Morosov, A. Nawrot, B. Nefkens, G. Norman, W. Oelert, C. Pauly, H. Pettersson, A. Pivovarov, J. Pätzold, Y. Petukhov, A. Povtorejko, D. Reistad, R. Ruber, S. Sandukovsky, K. Schönning, W. Scobel, T. Sefzick, R. Shafigullin, B. Schwartz, V. Sidorov, T. Skrodsk, V. Sopo, A. Starostin, J. Stepaniak, A. Sukhanov, A. Sukhano, V. Tchernyshev, P. Tegner, P. T. Engblom, V. Tikhomirov, H. Toki, A. Turowieck, G. Wagner, U. Wiedner, Z. Wilhelmi, M. Wolk, A. Yamamoto, H. Yamaoka, J. Zabierowski, I. Zartova, and J. Złomańczuk, Nucl. Instrum. Methods Phys. Res., Sect.A **594**, 339 (2008).
- [27] B.Hoistad, J.Ritman, *et al.*, arXiv:nucl-ex/0411038 (2004).
- [28] B. Klos *et al.*, Few-Body Syst. **65**, 21 (2024).
- [29] P. Vlasov, *Analysis of the $\eta \rightarrow 3\pi^0$ decay in the pp interaction*, Ph.D. thesis, Ruhr - Universitat Bochum, Germany (2008).
- [30] A. Ramazani-Moghaddam-Arani, *Cross section and analyzing power measurements in three and four-nucleon scattering*, Ph.D. thesis, RUG (2009).
- [31] K. Ermisch, H. R. Amir-Ahmadi, A. M. v. d. Berg, R. Castelijns, B. Davids, A. Deltuva, E. Epelbaum, W. Glöckle, J. Golak, M. N. Harakeh, M. Hunyadi, M. A. d. Huu, N. Kalantar-Nayestanaki, H. Kamada, M. Kiš, M. Mahjour-Shafiei, A. Nogga, P. U. Sauer, R. Skibiński, H. Witała, and H. J. Wörtche, Phys. Rev. C **68**, 51001(R) (2003).
- [32] K. Ermisch, H. R. Amir-Ahmadi, A. M. v. d. Berg, R. Castelijns, B. Davids, A. Deltuva, E. Epelbaum, W. Glöckle, J. Golak, M. N. Harakeh, M. Hunyadi, M. A. d. Huu, N. Kalantar-Nayestanaki, H. Kamada, M. Kiš, M. Mahjour-Shafiei, A. Nogga, P. U. Sauer, R. Skibiński, H. Witała, and H. J. Wörtche, Phys. Rev. C **71**, 064004 (2005).
- [33] K. Kuroda, A. Michalowicz, and M. Poulet, Phys. Lett. **13**, 67 (1964).
- [34] R. Machleidt, F. Sammarruca, and Y. Song, Phys. Rev. C **53**, R1483 (1996).
- [35] R. Machleidt, Phys. Rev. C **63**, 024001 (2001).
- [36] S. A. Coon and W. Glöckle, Phys. Rev. C **23**, 1790 (1981).
- [37] W. Glöckle and S. A. Coon, Phys. Rev. C **23**, 1790 (1981).
- [38] R. B. Wiringa, V. G. J. Stoks, and R. Schiavilla, Phys. Rev. C **51**, 10.1103/PhysRevC.51.38 (1995).
- [39] V. Stoks, R. Klomp, C. Terheggen, and J. de Swart, Phys. Rev. C **49**, 2950 (1994).
- [40] A. Deltuva, K. Chmielewski, and P. U. Sauer, Phys. Rev. C **67**, 034001 (2003).

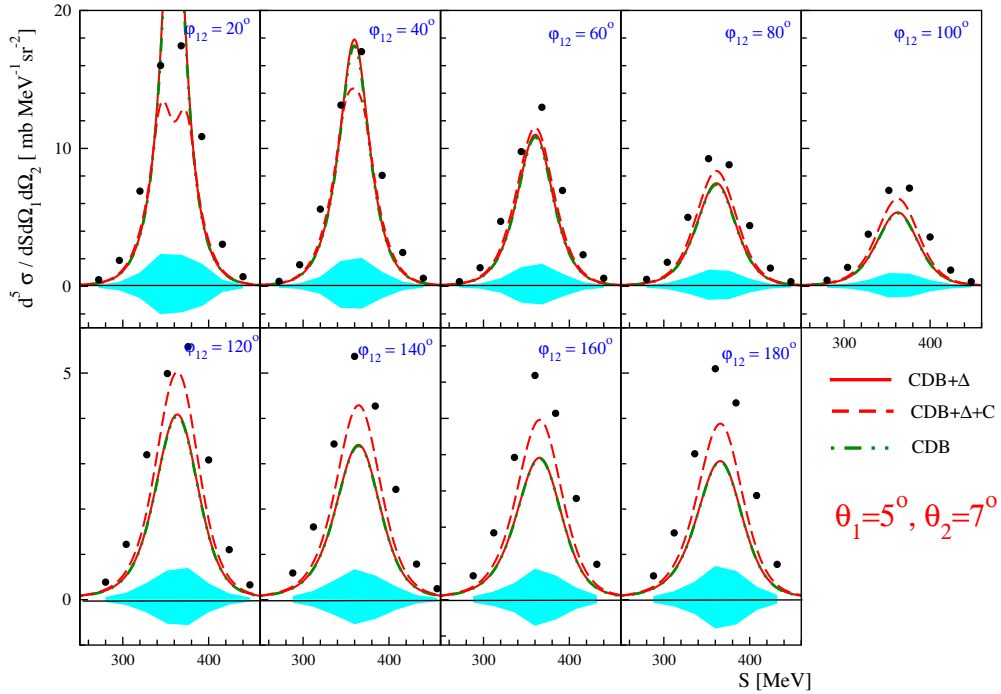
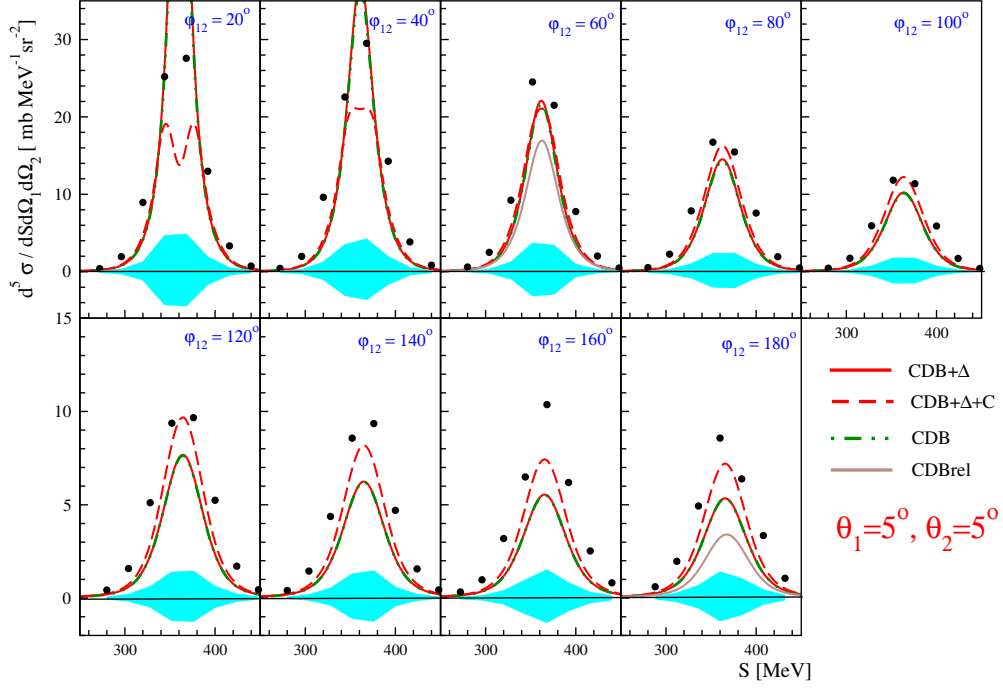


FIG. 11. (Color online) Differential cross section of ${}^1\text{H}(d, pp)n$ breakup reaction at beam energy of 190 MeV/nucleon shown in function of S variable. The presented data belong to 9 kinematic configurations characterised with the same combinations of proton polar angles ($\theta_1=5^\circ$, $\theta_2=5^\circ$ in the top part and $\theta_1=5^\circ$, $\theta_2=7^\circ$ in the bottom part) and various relative azimuthal angles of the two protons, indicated in the individual panels. Statistical errors are smaller than the size of the points. Systematic uncertainties are represented by bands. Theoretical calculations are shown as lines specified in the legend.

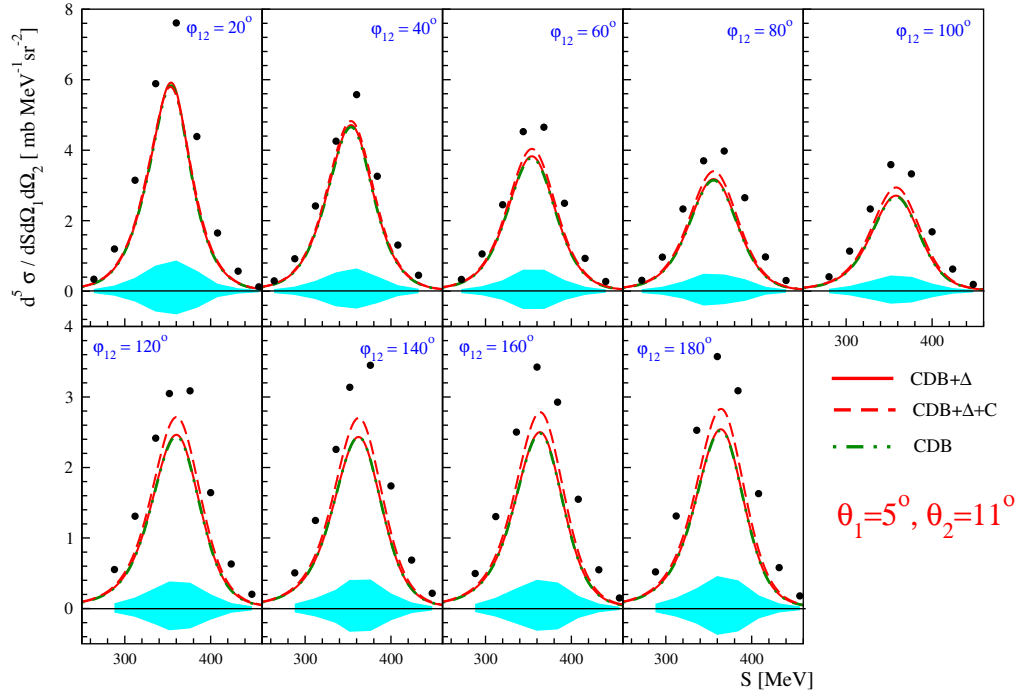
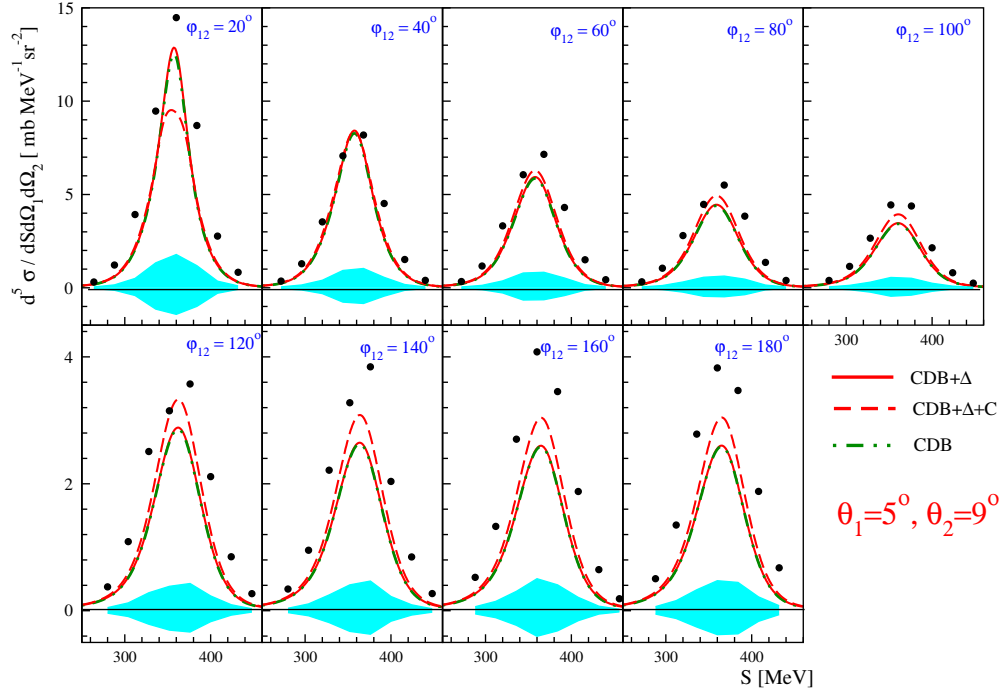


FIG. 12. (Color online) The same as Fig. 11 but for kinematic configurations with the proton polar angles $\theta_1 = 5^\circ$, $\theta_2 = 9^\circ$ and $\theta_1 = 5^\circ$, $\theta_2 = 11^\circ$.

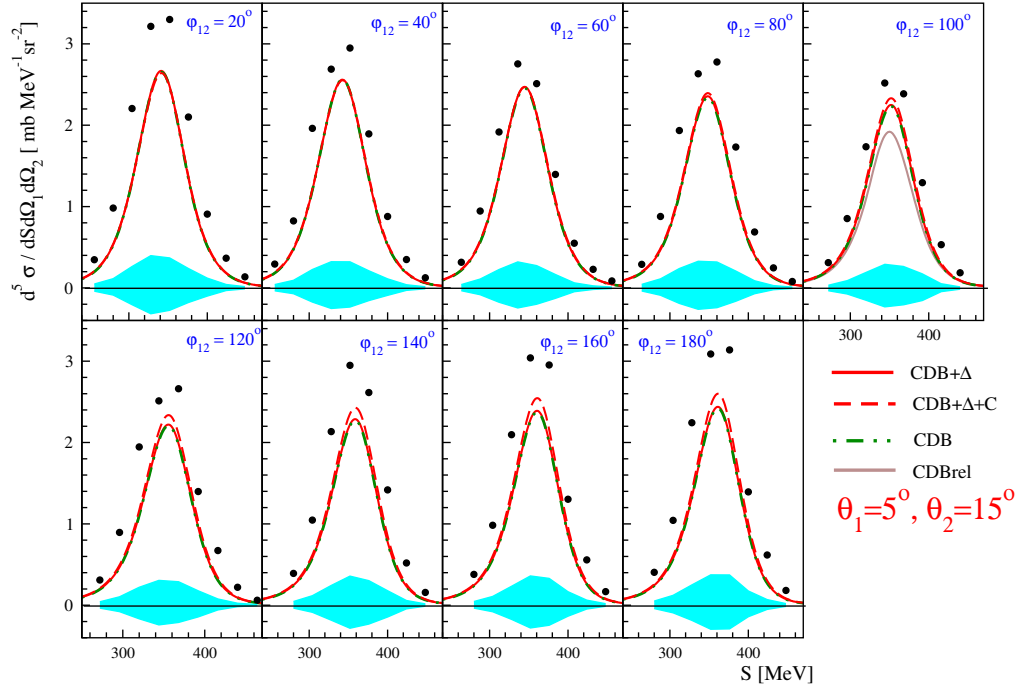
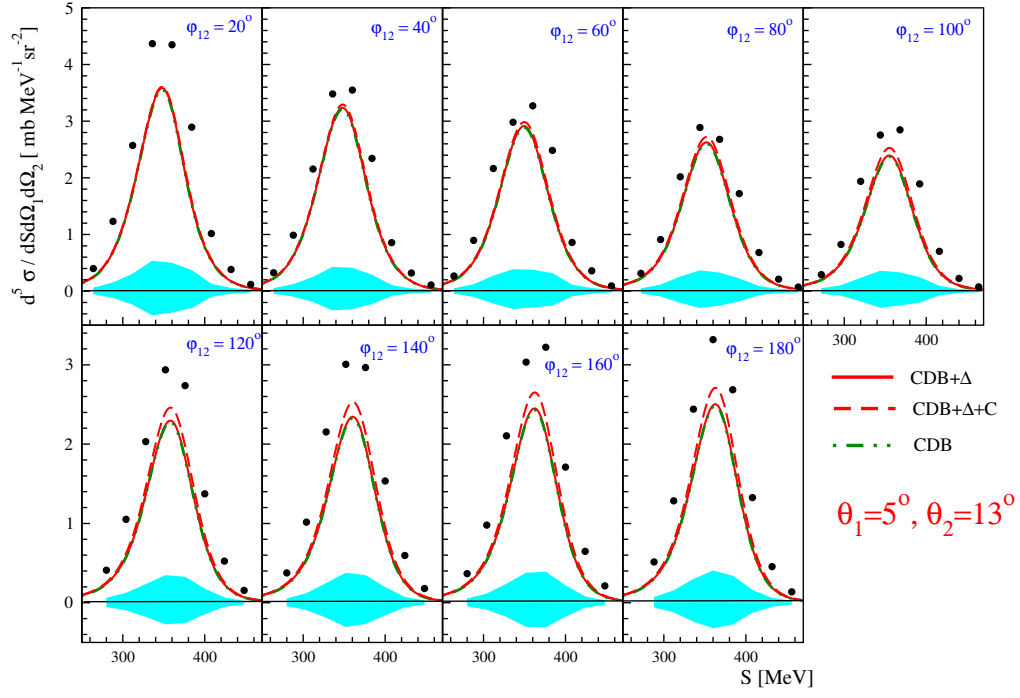


FIG. 13. (Color online) The same as Fig. 11 but for kinematic configurations with the proton polar angles $\theta_1 = 5^\circ$, $\theta_2 = 13^\circ$ and $\theta_1 = 5^\circ$, $\theta_2 = 15^\circ$.

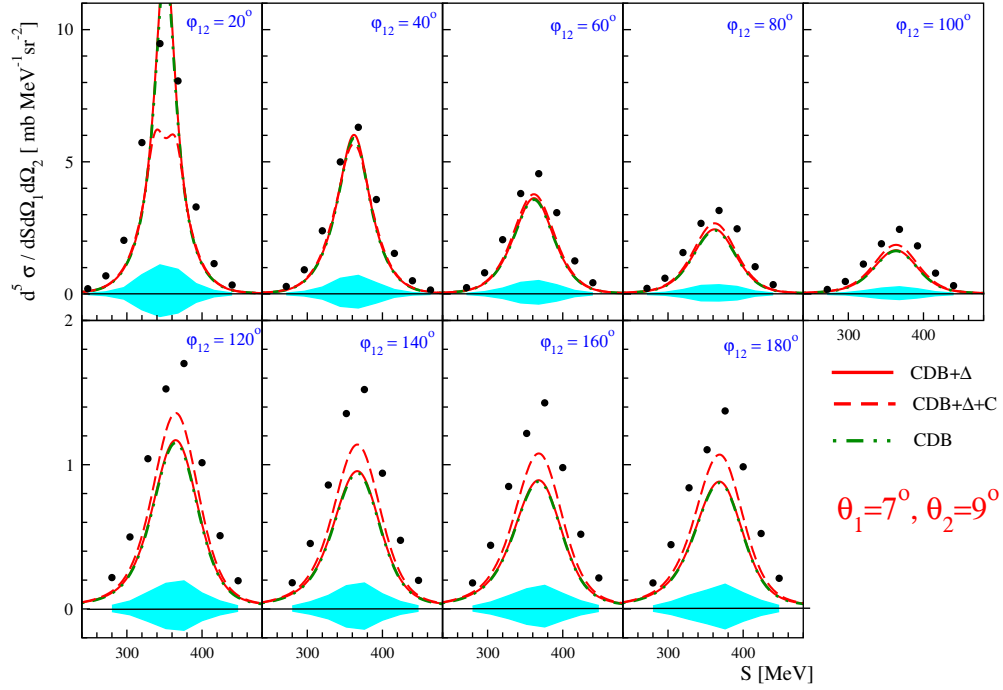
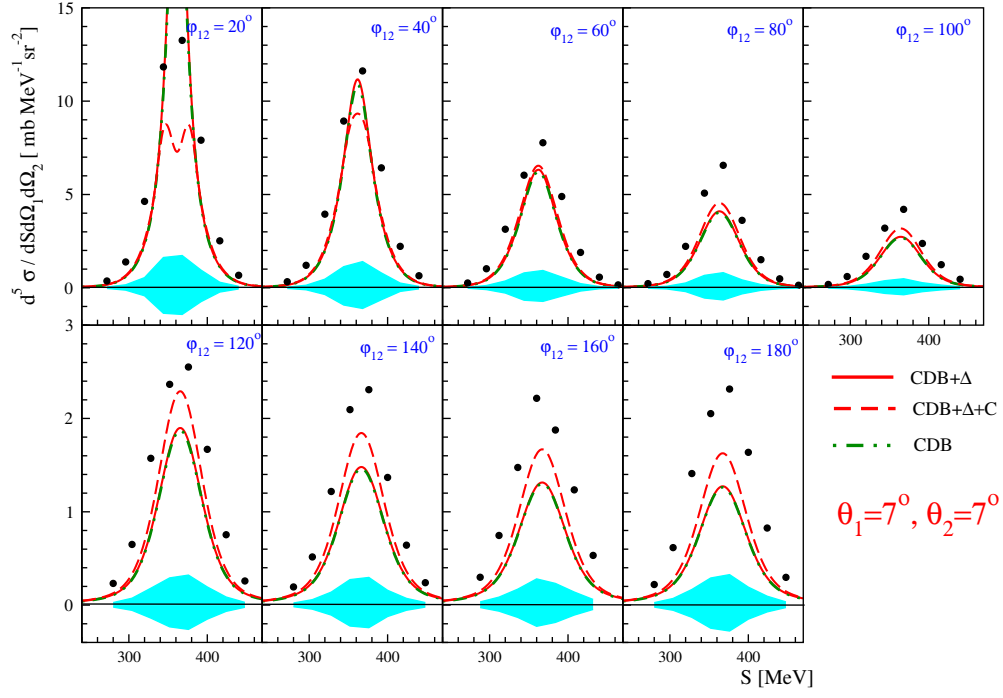


FIG. 14. (Color online) The same as Fig. 11 but for kinematic configurations with the proton polar angles $\theta_1 = 7^\circ$, $\theta_2 = 7^\circ$ and $\theta_1 = 7^\circ$, $\theta_2 = 9^\circ$.

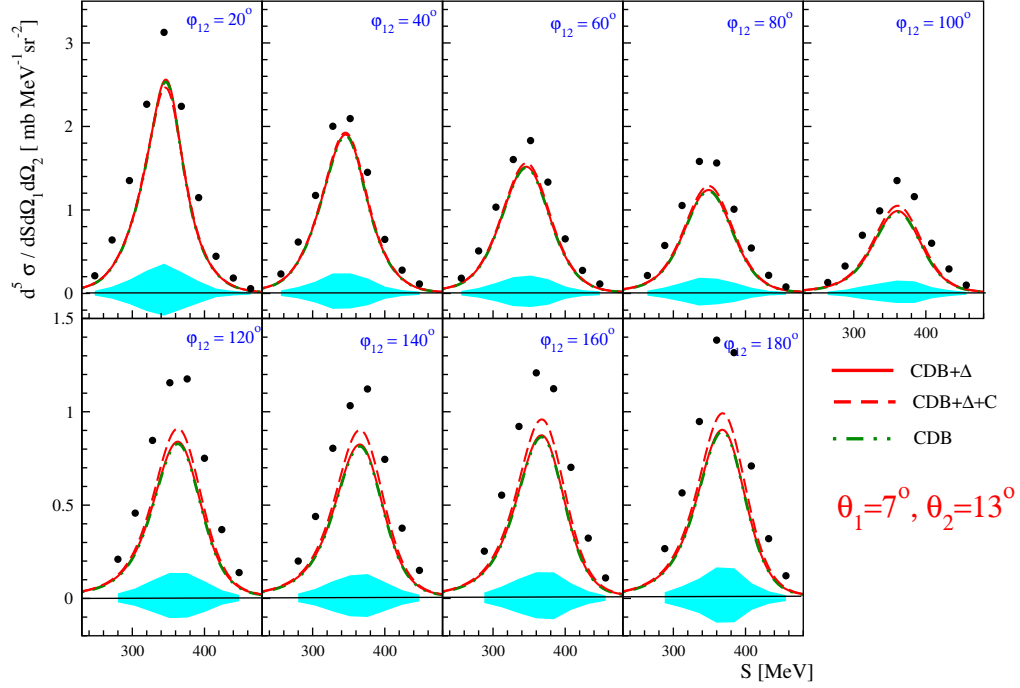
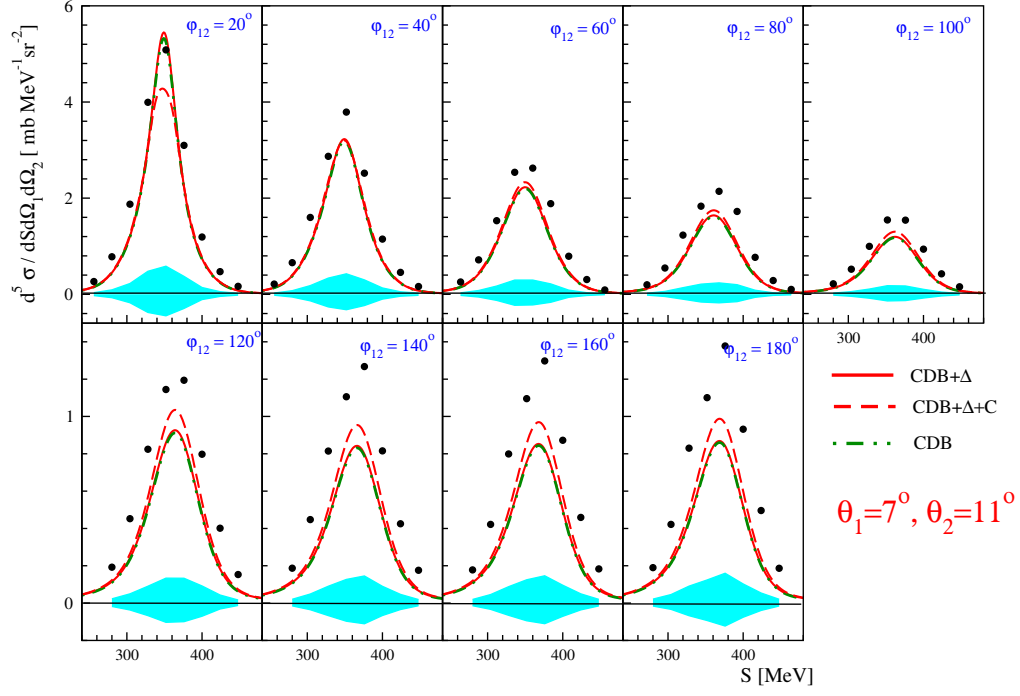


FIG. 15. (Color online) The same as Fig. 11 but for kinematic configurations with the proton polar angles $\theta_1=7^\circ$, $\theta_2=11^\circ$ and $\theta_1=7^\circ$, $\theta_2=13^\circ$.

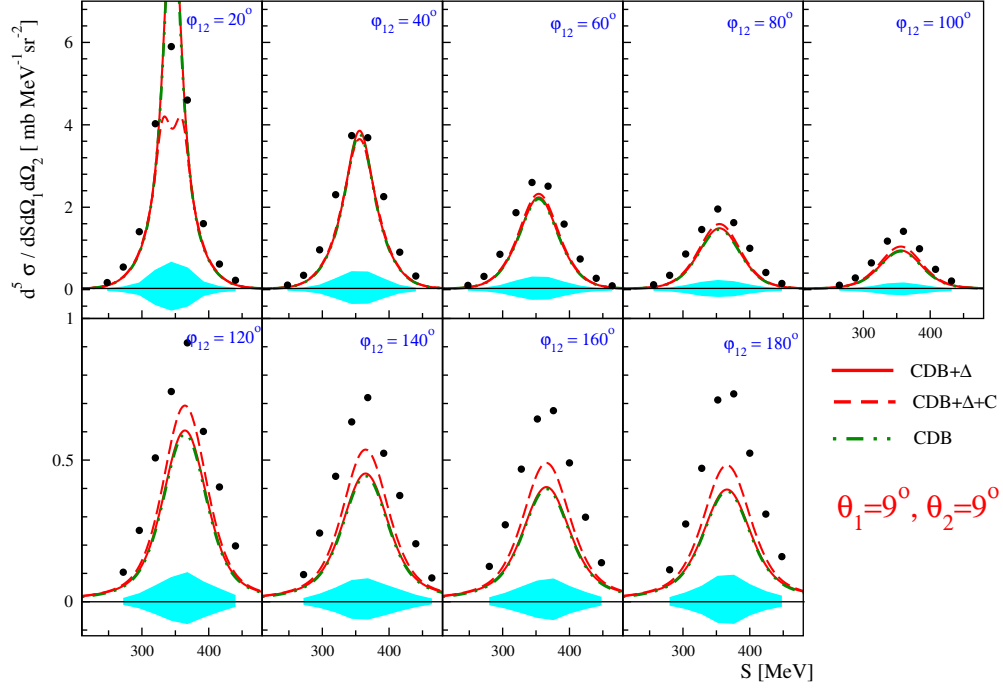
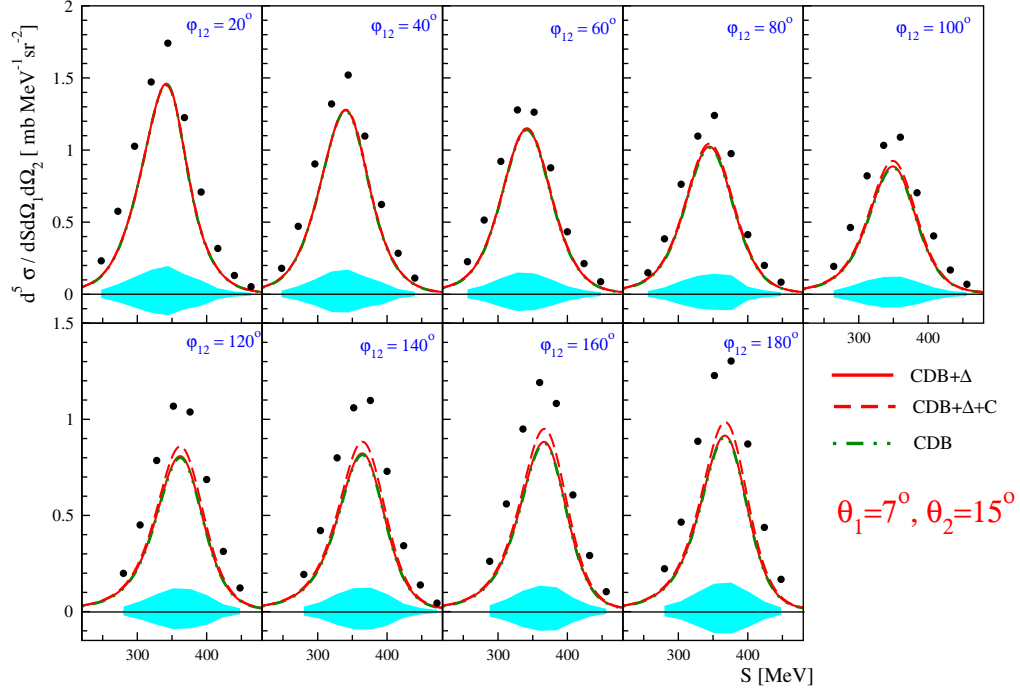


FIG. 16. (Color online) The same as Fig. 11 but for kinematic configurations with the proton polar angles $\theta_1 = 7^\circ$, $\theta_2 = 15^\circ$ and $\theta_1 = 9^\circ$, $\theta_2 = 9^\circ$.

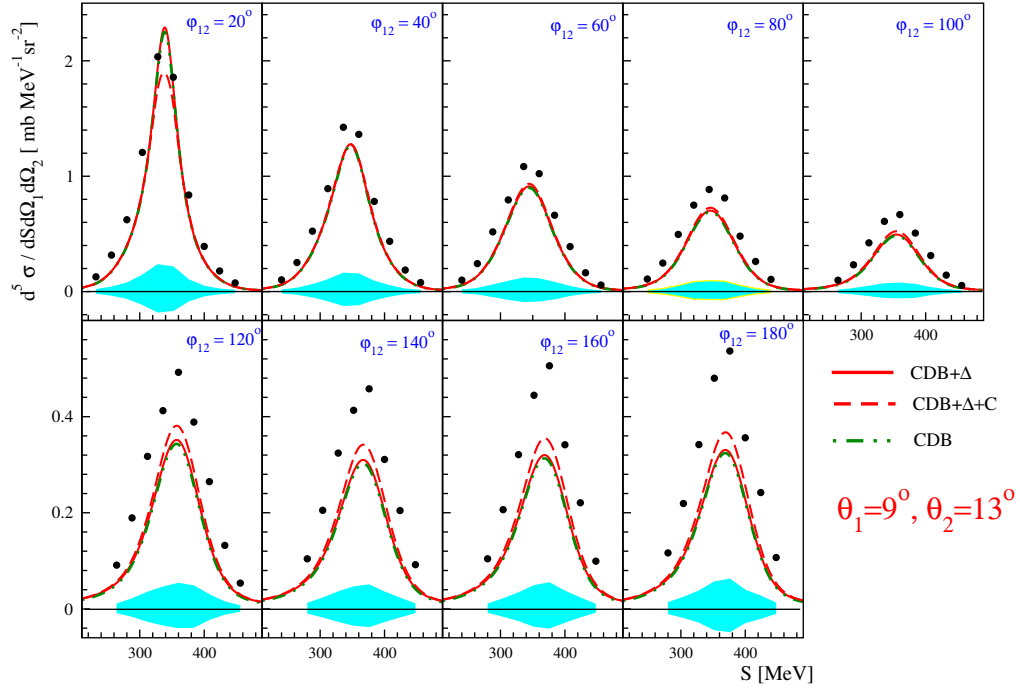
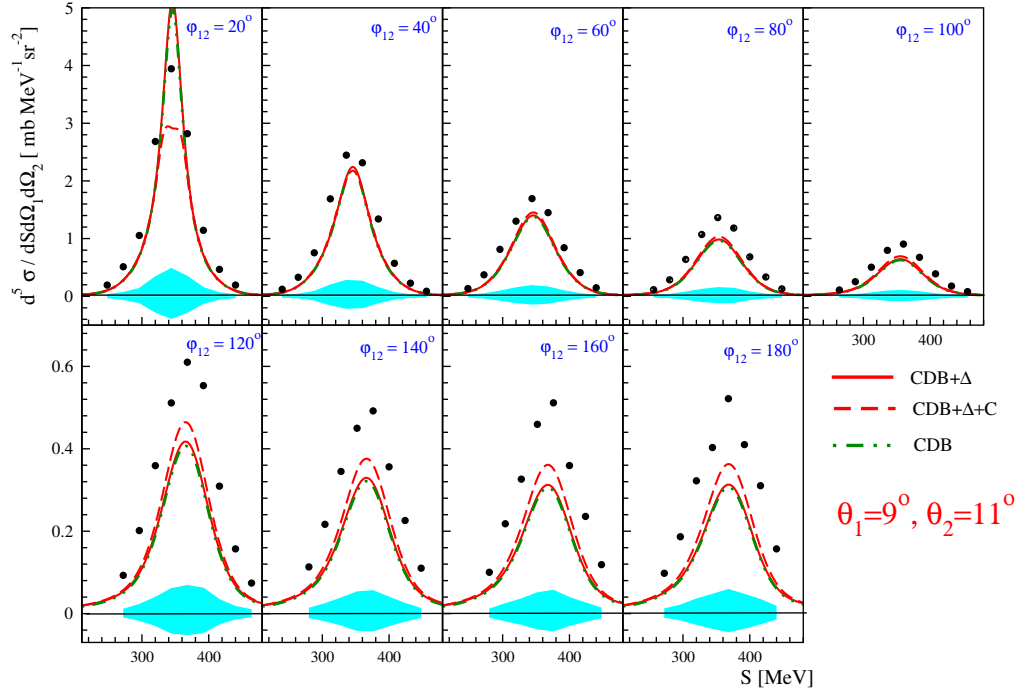


FIG. 17. (Color online) The same as Fig. 11 but for kinematic configurations with the proton polar angles $\theta_1=9^\circ, \theta_2=11^\circ$ and $\theta_1=9^\circ, \theta_2=13^\circ$.

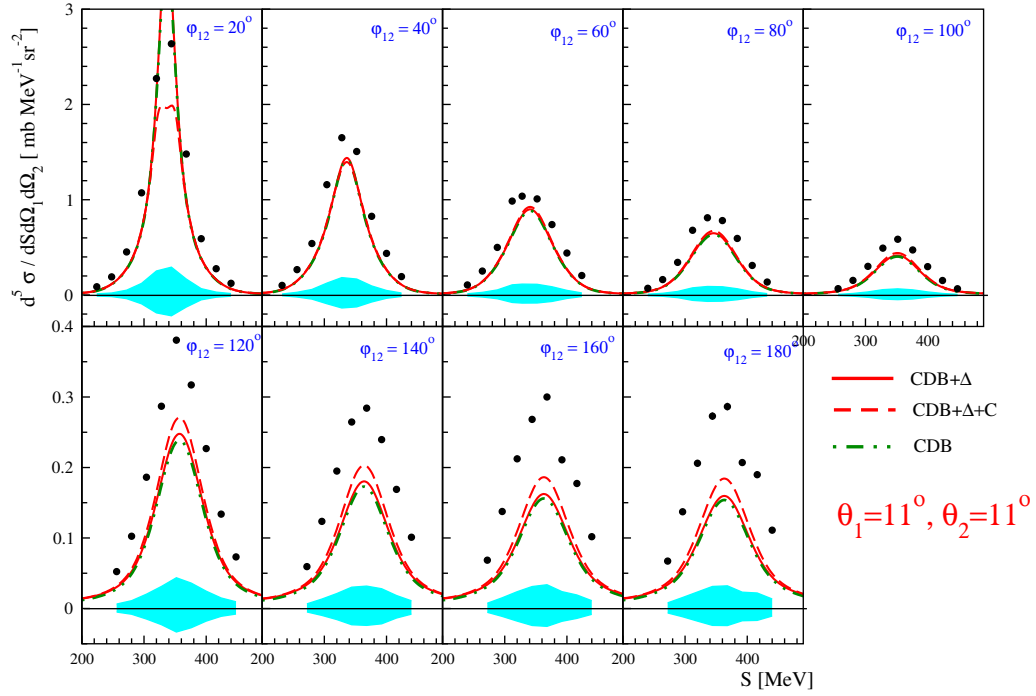
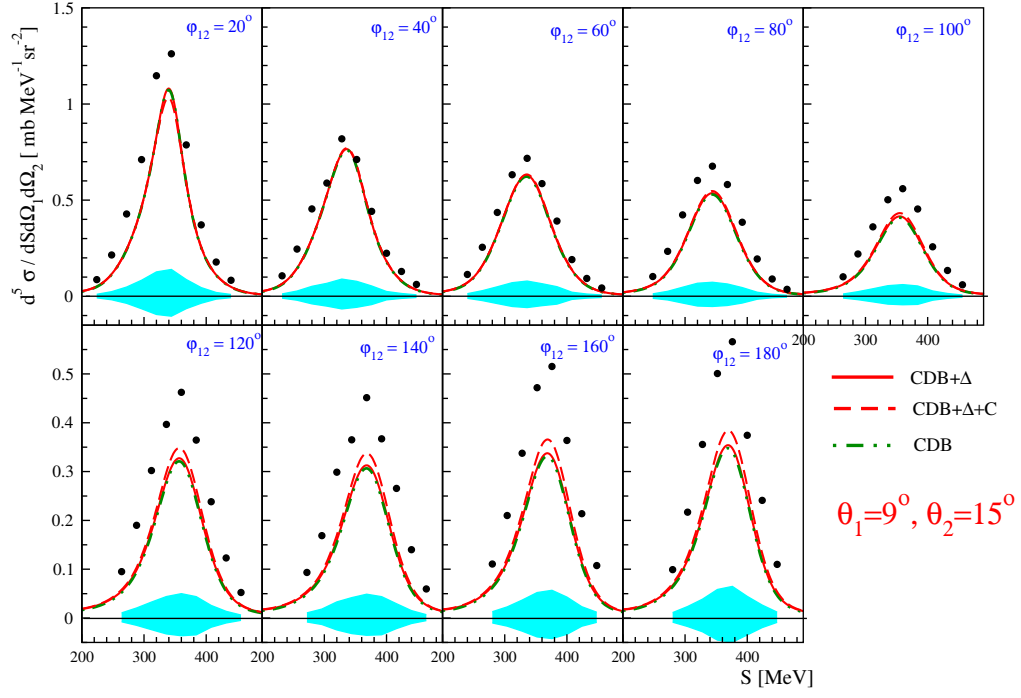


FIG. 18. (Color online) The same as Fig. 11 but for kinematic configurations with the proton polar angles $\theta_1 = 9^\circ, \theta_2 = 15^\circ$ and $\theta_1 = 11^\circ, \theta_2 = 11^\circ$.

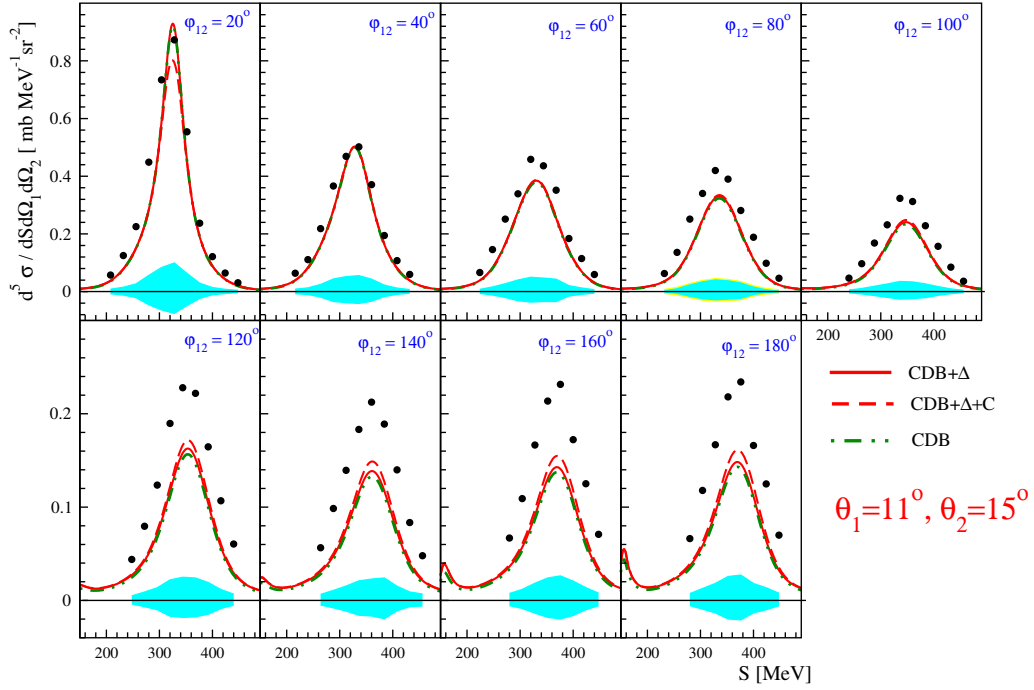
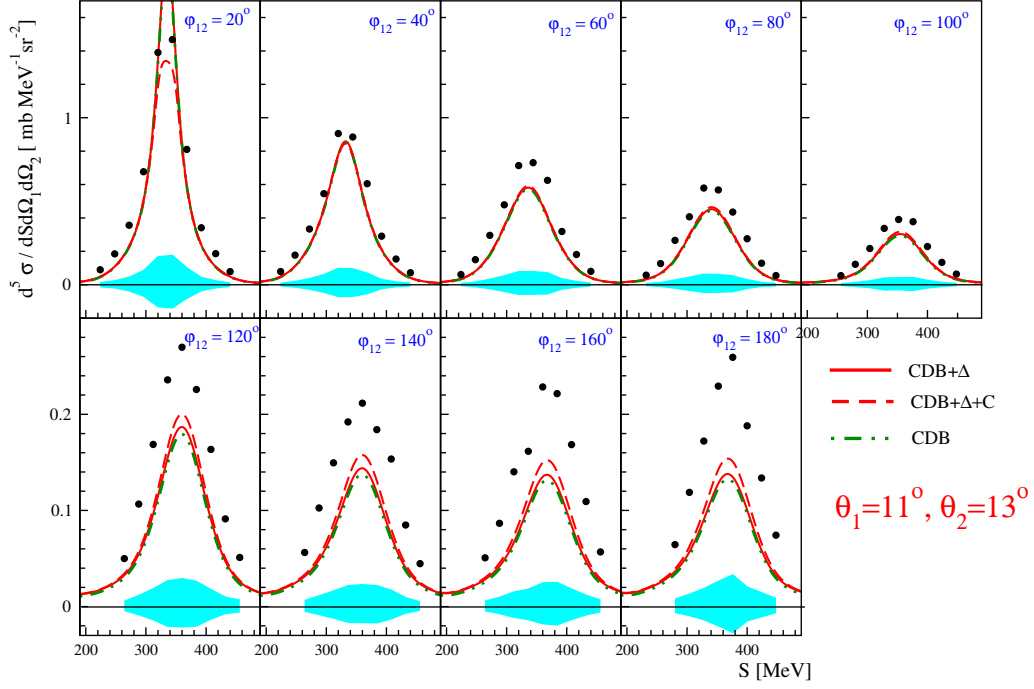


FIG. 19. (Color online) The same as Fig. 11 but for kinematic configurations with the proton polar angles $\theta_1 = 11^\circ, \theta_2 = 13^\circ$ and $\theta_1 = 11^\circ, \theta_2 = 15^\circ$.

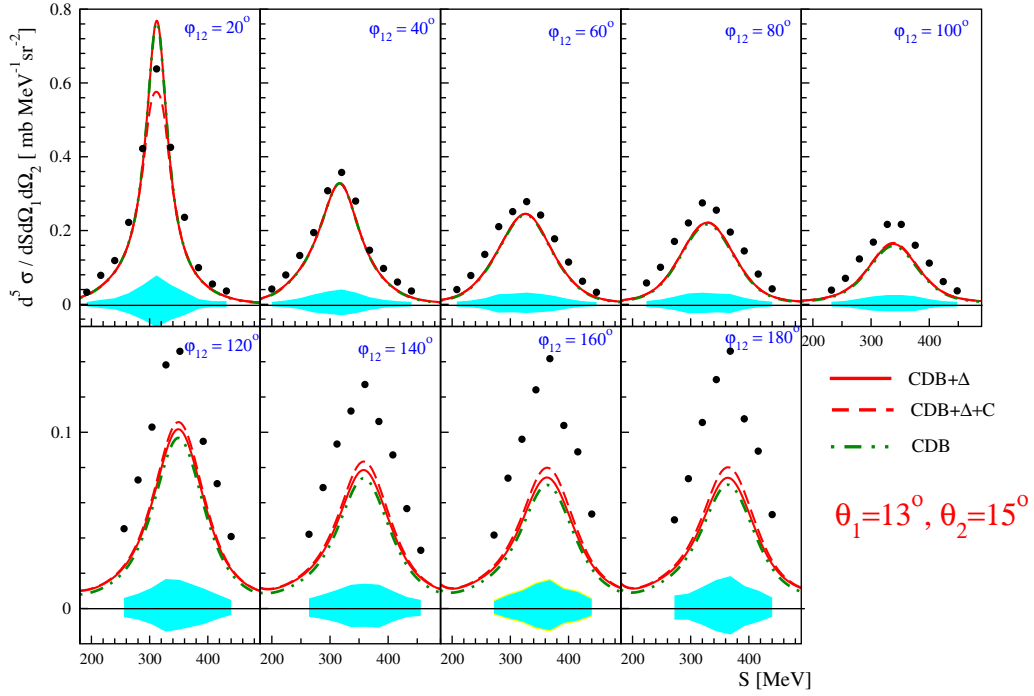
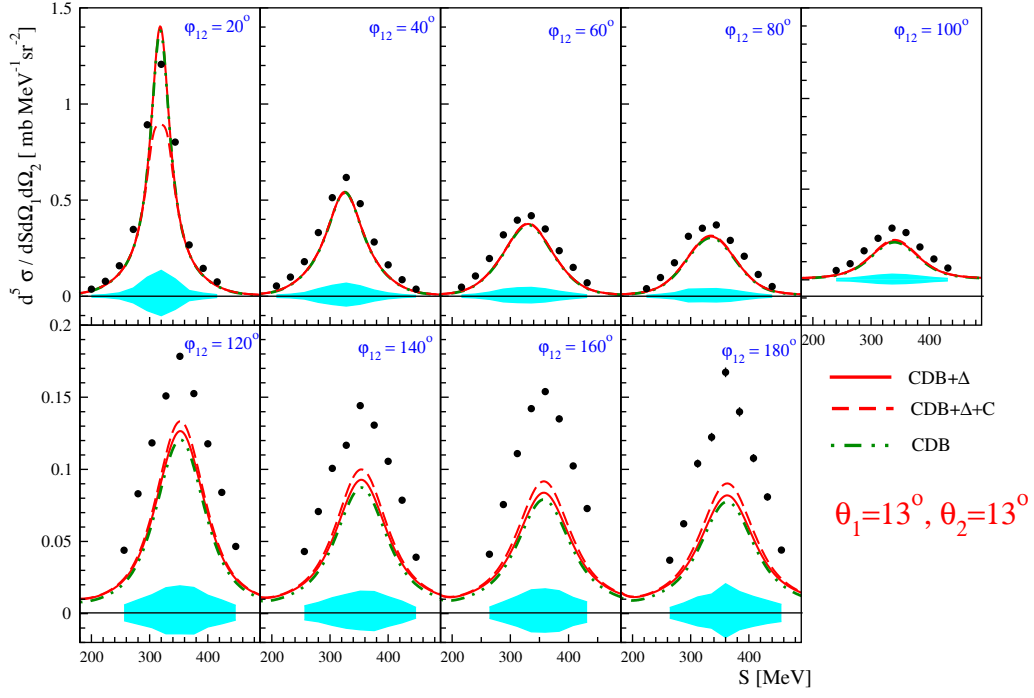


FIG. 20. (Color online) The same as Fig. 11 but for kinematic configurations with the proton polar angles $\theta_1 = 13^\circ$, $\theta_2 = 13^\circ$ and $\theta_1 = 13^\circ$, $\theta_2 = 15^\circ$.

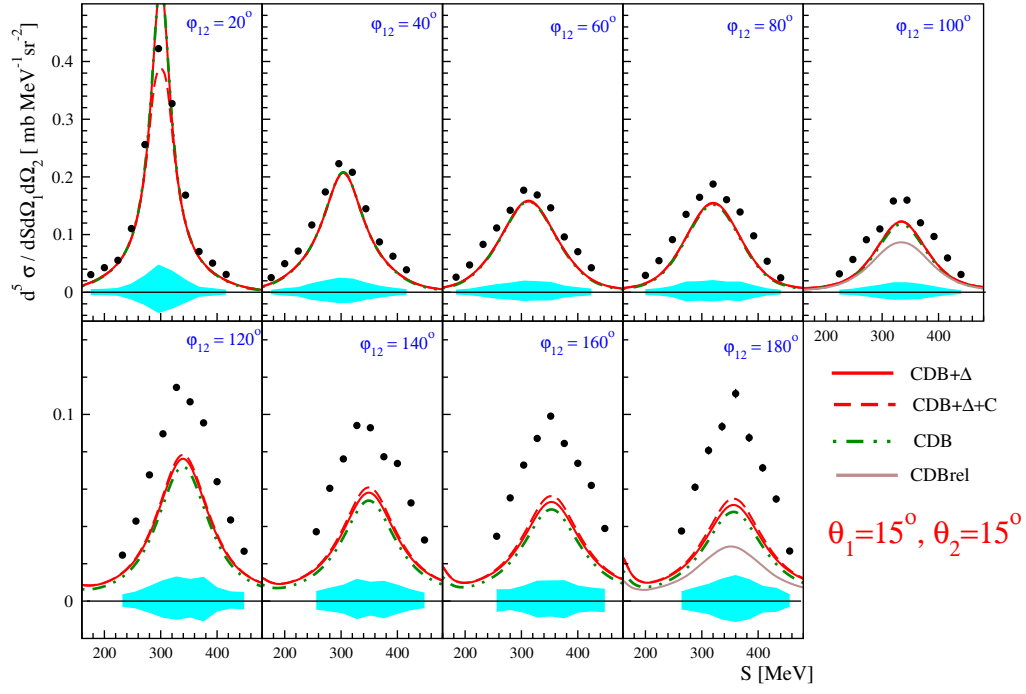


FIG. 21. (Color online) The same as Fig. 11 but for kinematic configurations with proton polar angles $\theta_1 = 15^\circ, \theta_2 = 15^\circ$.